Magmatic volatile budgets of the 2014 Tavurvur eruption at Rabaul Caldera, Papua New Guinea

Melina Höhn[a *], Brendan McCormick Kilbride[a], Margaret Hartley[a], Mike Burton[a], John B. Dikaung[b], Ben Esse[a], Ima Itikarai[b], Kila Mulina[b], Steve Saunders[b], Mikhail Sindang[b], Isabelle A. Taylor[c], EIMF[d]

[a]*Department of Earth and Environmental Sciences, University of Manchester, Manchester, M13 9PL, United Kingdom*

[b]*Rabaul Volcano Observatory, P.O. Box 386, Rabaul, East New Britain Province, Papua New Guinea*

[c]*COMET Atmospheric, Oceanic and Planetary Physics, University of Oxford, Oxford, OX1 3PU, United Kingdom*

[d]*Edinburgh Ion Microprobe Facility, School of GeoSciences, University of Edinburgh, EH9 3FE, United Kingdom*

*Corresponding author. E-mail address: melina1995.hoehn@gmail.com

This is a non-peer reviewed preprint submitted to EarthArXiv in January 2026. It has also been submitted for publication to *Journal of Volcanology and Geothermal Research* and is currently under review. Subsequent versions may differ.

Magmatic volatile budgets of the 2014 Tavurvur eruption at Rabaul Caldera, Papua New Guinea

Melina Höhn[a *], Brendan McCormick Kilbride[a], Margaret Hartley[a], Mike Burton[a], John B. Dikaung[b], Ben Esse[a], Ima Itikarai[b], Kila Mulina[b], Steve Saunders[b], Mikhail Sindang[b], Isabelle A. Taylor[c], EIMF[d]

[a]*Department of Earth and Environmental Sciences, University of Manchester, Manchester, M13 9PL, United Kingdom*

[b]*Rabaul Volcano Observatory, P.O. Box 386, Rabaul, East New Britain Province, Papua New Guinea*

[c]*COMET Atmospheric, Oceanic and Planetary Physics, University of Oxford, Oxford, OX1 3PU, United Kingdom*

[d]*Edinburgh Ion Microprobe Facility, School of GeoSciences, University of Edinburgh, EH9 3FE, United Kingdom*

*Corresponding author. E-mail address: melina1995.hoehn@gmail.com

---

Abstract

Rabaul is a caldera volcano on New Britain Island, Papua New Guinea, whose active cone Tavurvur ranks seventh globally for long-term SO_2 and CO_2 emissions. It is unknown why Rabaul is such a strong emitter of volcanic gases. Magma mixing between basaltic and dacitic magmas is envisioned to play a fundamental role in driving eruptions at Rabaul, but the

compositions of mafic recharge magmas and their contribution to ongoing gas emissions are poorly constrained. We analysed 87 plagioclase-, clinopyroxene- and olivine-hosted melt inclusions from 2014 Tavurvur volcanic bombs for major, trace and volatile elements (H_2O, CO_2, SO_2, Cl, F), corrected for post-entrapment crystallisation, and combined these data with satellite-derived SO_2 retrievals (OMI, IASI) and plume-trajectory modelling. Olivine- and high-Mg# clinopyroxene-hosted melt inclusions record basaltic compositions likely representing the mafic recharge magmas of the volcanic system. Low-An plagioclase- and low-Mg# clinopyroxene-hosted melt inclusions are andesitic to dacitic in composition which closely match dacites erupted at Rabaul (Rabaul Pyroclastics) and likely record the composition of magma resident in Rabaul's shallow plumbing system. Reverse fractional crystallization and trace element constraints imply primary volatile contents of ~1.1–1.9 wt% H_2O, 1400–2600 ppm SO_2, ~392 ppm Cl and ~59 ppm F, indicating Rabaul magmas are not anomalously volatile-rich compared to those generated in other subduction zones with an intermediate slab thermal parameter. Our analyses of OMI and IASI satellite data yield an SO_2 mass of ~17–19 kt for the 2014 eruption; petrological estimates derived from our melt inclusion analyses give ~21 kt. We attribute the modest 2014 SO_2 release to low erupted magma volumes and extensive pre-eruptive degassing of the shallow reservoir between 2006–2010, and note that volatile-rich mafic magma was volumetrically minor in the erupted material. Our results reconcile melt-inclusion and satellite records and constrain the roles of magma mixing and prior degassing in governing Rabaul's gas output.

Keywords: Melt Inclusions, Volatile budgets, Rabaul, SO_2 emissions, OMI, IASI

1. Introduction

Melt inclusions are small pockets of silicate melt trapped within crystals as they form in magmatic systems. Melt inclusions preserve a record of the magmatic conditions at the time of their formation because they are isolated from the external environment once they are trapped within the host crystal (Frezzotti, 2001; Rose-Koga et al., 2021, and references therein). This encapsulation can protect them from subsequent magmatic processes such as mixing, contamination, or magma degassing which can alter the bulk magma composition (Schiano, 2003; Wallace, 2005; Wallace et al., 2015; Venugopal et al., 2020a). Thus, the study of melt inclusions provides critical insights into the conditions of magma formation, evolution, and the pre-eruptive history of volcanic systems (Kent, 2008; Metrich and Wallace, 2008; Ruth et al., 2018). Melt inclusions are particularly valuable for constraining the pre-eruptive volatile content of magmas because they may trap magmatic volatiles before significant degassing occurs (Lowenstern, 2003; Wallace, 2005; Wallace and Edmonds, 2011). Additionally, melt inclusions can be analysed in-situ within their host minerals, providing context for the conditions of magma evolution and storage especially in situations where erupted magmas show evidence of having accumulated batches of crystals from multiple storage reservoirs (Aster et al., 2016; Zhang et al., 2019; Rose-Koga et al., 2021).

Volatiles such as H_2O, CO_2, and SO_2 strongly control magmatic behaviour and evolution. Dissolved volatiles reduce melt viscosity, depress liquidus temperatures and shift phase equilibria, and thereby change magma rheology, density and the thermal budget during ascent (e.g., Huppert and Woods, 2002; Wallace and Edmonds, 2011; Wallace et al., 2015; Edmonds and Wallace, 2017; La Spina et al., 2022). During decompression, H_2O and CO_2 exsolve according to pressure-, temperature-, and composition-dependent solubility relations. These

solubility relations set the pressure (depth) of first bubble saturation and dictate whether degassing proceeds in an open, continuous manner or in a closed, batch-like manner that permits accumulation of a distinct vapour phase (e.g. Edmonds and Woods, 2018; Scholz et al., 2023). The rate and style of volatile exsolution and degassing is controlled by bubble nucleation and growth kinetics. When bubble growth and expansion outpace gas escape and melt relaxation, internal overpressure and tensile stresses may exceed melt strength and induce brittle fragmentation and explosive eruption, whereas efficient bubble percolation and permeable flow limit overpressure and favour less explosive behaviour. (Tait et al., 1989; La Spina et al., 2022). Quantifying pre-eruptive volatile budgets and understanding their solubility-mediated behaviour is therefore essential for assessing eruption style, explosivity and the degassing history of volcanic systems.

Rabaul is a large caldera system characterised by a long and complex eruption history (Heming, 1974; Nairn et al., 1995; Wood et al., 1995; Patia, 2004). Satellite observations from 2005–2015 showed that high SO_2 outgassing at Tavurvur occurred between late 2006 and late 2009 of up to 6–7 kt per day, even though Tavurvur showed mild, intermittent volcanic activity during this timeframe, but no powerful explosive eruptions (McCormick et al., 2012; Carn et al., 2017). This high outgassing placed Tavurvur seventh overall in the world for both SO_2 emissions during this interval, with long term mean fluxes of ~1700 t SO_2 per day (Carn et al., 2017). Aiuppa et al. (2019) estimated coincident mean CO_2 emission rates of 3000 t per day, based on global correlations between whole rock Ba/La ratios and volcanic gas plume CO_2/S_T ratios, placing Tavurvur seventh globally for CO_2 flux, too. However, the most recent eruption at Rabaul in 2014 was accompanied by comparatively low SO_2 emissions of ~18 kt (S. Carn, OMI satellite, Global Volcanism Program, 2014), which is only a fraction of the SO_2 emitted during the 1994 (~350 kt) and 2006 (~230 kt) eruptions (Bouvet de Maisonneuve et al., 2015;

Rose et al., 1995). This leads to the question: What was the pre-eruptive volatile content of magmas involved in the 2014 eruption? Notably, Saunders et al. (2023) measured only limited ground deformation during the 2014 eruption and suggested on this basis that the 2014 event may have only involved the explosion of a conduit plug and the eruption of already degassed magma. Melt inclusions present a promising tool to constrain these volatile contents.

Volcanic activity at Rabaul is sustained through regular mafic recharge, as evidenced by the finding of basaltic enclaves in the form of distinctly mafic mineral clots and mafic macrocrysts (Bouvet de Maisonneuve et al., 2015; Patia et al., 2017; Fabbro et al., 2020; Höhn et al., 2026). Modelling results show mixing between a recharge magma with a composition similar to basaltic enclaves found in the 1937 eruption products and a resident dacite with a composition similar to the products of the last caldera-forming eruption (Patia, 2004; Patia et al., 2017; Fabbro et al., 2020; Höhn et al., 2026;). The limited basaltic enclaves are the only constraint on the composition of the mafic recharge magma so far. The question remains what the actual chemical composition of the mafic recharge magma is.

We have studied the crystal cargo of historical Rabaul eruption products and developed a classification for the different minerals based on their compositions and zoning patterns (Höhn et al., 2026). Our study revealed that olivine, high-An plagioclase and high-Mg# clinopyroxene are out of equilibrium with their carrier melt, and instead are likely to have crystallised from a more mafic magma, potentially the recharge magma, before being mixed into a more evolved magma prior to eruption. In contrast, low-An plagioclase and low-Mg# clinopyroxene are in equilibrium with, and probably crystallised from the more evolved, dacitic magma. Melt inclusions hosted in these minerals capture the composition of the magmas from which they crystallised, offering a means to analyse direct samples of the mafic recharge magma to further

constrain its chemical characteristics. Moreover, these melt inclusions give us the opportunity to evaluate the volatile content of diverse magmas present in the Rabaul magma plumbing system.

In this study, we analysed plagioclase-, clinopyroxene- and olivine-hosted melt inclusions from volcanic bombs erupted in 2014 at Rabaul. Our study aims to constrain melt and volatile (H_2O, CO_2, SO_2, Cl, F) compositions of the magmas these minerals crystallised from, to constrain the volatile budget prior to and during the 2014 eruption. We use volatile-trace element ratios to calculate the volatile contents of the primary Rabaul magma and compare our results with the global spectrum of primary arc magmas. Lastly, we calculate the mass of SO_2 released during the 2014 eruption from both satellite-derived data and our melt inclusion data and contextualise this SO_2 budget for the 2014 eruption within the broader Rabaul eruption sequence from 1994 to the present.

2. Geological background

2.1 Tectonic and geographic background

The Rabaul Caldera is situated within a complex tectonic environment, governed by the convergence of the Pacific plate and the Australian plate (Fig. 1a) (Baldwin et al., 2012; Holm et al., 2016). This region is characterised by complex regional kinematics including the accommodation of multiple subduction zones. This has resulted in the formation of several regional microplates, among them the North and South Bismarck plates and the Solomon Sea plate (Holm et al., 2016). Present day volcanism along the New Britain Island is sustained through subduction of the Solomon Sea microplate underneath the South Bismarck microplate. (Baldwin et al., 2012; Holm et al., 2016).

The Rabaul Caldera Complex is located at the eastern end of New Britain. The caldera itself is predominantly sea-filled, elliptical in shape, and measures ~14×9 km, with a prominent 5 km-wide breach in its southeastern section (Heming, 1974; Nairn et al., 1995). The region surrounding the caldera is home to a substantial population, with approximately 3,300 people residing within 5 km of the complex and an estimated 252,000 individuals living within a 100 km radius (Global Volcanism Program, 2013). The north-eastern to eastern sector of the caldera is bordered by two well-preserved stratovolcanoes, Kombiu and Turangunan, as well as the breached volcanic structure of Palangiangia, within which the younger cone, Rabalanakaia, has developed (Fig. 1b). The northern caldera wall features the deeply dissected volcanic cone of Tovanumbatir (Heming, 1974; McKee and Duncan, 2016). Kombiu, Turangunan, and Tovanumbatir are part of the Watom-Turangunan-Zone (WTZ-Zone), a northwest-southeast trending zone of predominantly mafic stratovolcanoes (Heming, 1974; McKee and Duncan, 2016).

Within the caldera itself, post-caldera volcanic activity has produced several distinct features. These include the Tavurvur cone in the east and the Vulcan cone in the west (Fig. 1b). Both contribute to the region's active and evolving geological landscape (Heming, 1974; Nairn et al., 1989; Nairn et al., 1995; Patia, 2004).

Volcanism at Rabaul commenced >330 kyr ago and included at least ten dacitic ignimbrite-producing eruptions, some of which were caldera-forming (McKee and Duncan, 2016; Nairn et al., 1995; Nairn et al., 1989; Wood et al., 1995). The most recent caldera-forming eruption took place between 667 and 699 CE (McKee et al., 2015) and its products are referred to as the Rabaul Pyroclastics (Nairn et al., 1989; Nairn et al., 1995; Wood et al., 1995). Since then, volcanic activity has been characterised by small- to medium-sized eruptions (VEI ≤4)

occurring at multiple vents across the caldera. The following text gives further details about the post-Rabaul Pyroclastics eruptions of which products are analysed in this study.

A twin eruption occurred in 1937 with Vulcan erupting on 29 May and Tavurvur following approximately 24 hours later (Patia, 2004). The eruption at Vulcan was sub-plinian, included some interaction with seawater and was assigned a VEI of four (Roggensack et al., 1996; Patia, 2004). A 255 m high cone was constructed during the eruption which linked the previous Vulcan Island to the mainland of New Britain. One day after volcanic activity at Vulcan had started, Tavurvur erupted in a small, discrete vulcanian event. The main phase of volcanic activity at both vents ended on 2 June but some individual, vulcanian events at Tavurvur were recorded until 1943 (Patia, 2004).

Rabaul experienced a significant seismic and deformational crisis from 1983 to 1985 (McKee et al., 1984; Mori and McKee, 1987). This seismic crisis commenced on 19 September 1983 and was characterised by frequent major seismic events involving hundreds of earthquakes in the space of less than one hour in intervals of 1 to 47 days. Additionally, a total uplift of approximately 50 mm was recorded at Matupit Island, and a second deformation source was identified in October 1983 on the eastern side of Vulcan (McKee et al., 1984). The combined seismic and deformational activity was believed to signal the injection of magma at a shallow depth and was thus interpreted as a potential precursor to an imminent eruption (McKee et al., 1984). However, both seismic and deformational activities steadily declined after June 1984, and no volcanic eruptions occurred (Mori and McKee, 1987).

The most recent phase of volcanic activity at the Rabaul Caldera began on 19 September of 1994 with another twin eruption. Volcanic activity at Vulcan was short-lived, ending on

2 October, and involved a plinian-style eruption, whereas the volcanic activity at Tavurvur comprised less powerful, but more sustained strombolian activity and a lava flow that was active from 12 to 25 October. The 1994 eruption resulted in the complete, although temporary, evacuation of nearby Rabaul Town (Global Volcanism Program, 1994; Johnson, 2013; Patia et al., 2017). Following intermittent eruptive activity of periodic explosions and small-to-moderate ash emissions with quiescence periods from weeks up to a year, a further eruption occurred at Tavurvur on 7 October 2006 (Global Volcanism Program, 2006). This eruption was characterised as sub-plinian with a tall ash column that rose into the tropopause and continued with strombolian eruptions with lava effusion after about 24 hours. The main phase of eruption ended on 8 October (Global Volcanism Program, 2006).

After this, Rabaul entered another phase of intermittent eruptive activity with periodic explosions and small-to-moderate ash emissions as well as occasional ejection of lava fragments. This activity was interspersed with weeks to several months of quiescence (Global Volcanism Program, 2007; Global Volcanism Program, 2013). Furthermore, from late 2006 onwards, Tavurvur experienced a major phase of SO_2 emissions which were not directly linked to any discrete eruptions (McCormick et al., 2012; Carn et al., 2017). The annual mean SO_2 flux measured by satellite increased from ~1 kt per day in late 2006 to almost 7 kt per day mid 2008. After that, SO_2 emissions declined again until mid 2010. From then on, very little SO_2 emissions were detected from Tavurvur (Carn et al., 2017).

The most recent eruption at Rabaul occurred in 2014 at Tavurvur. Volcanic activity started on 29 August with a strombolian eruption which included discrete explosions with ejections of volcanic bombs 500–1000 m from the crater, small lava fountains, and the creation of an 18 km high plume with extensive ash fall. An estimated 18 kt of SO_2 was emitted on 29 August

(S. Carn, OMI, Global Volcanism Program, 2014). This is about a tenth of the total SO_2 emission released during the 2006 eruption (Bouvet de Maisonneuve et al., 2015). Volcanic activity lasted about 24 hours before it died down. Smaller explosions followed until 30 August, but the volcano remained quiet after this except for another small explosion on 18 September and white, diffuse vapour emissions until December 2014 (Global Volcanism Program, 2017). No further volcanic activity was recorded at Rabaul since September 2014 except for periodic release of diffuse, white vapour (Global Volcanism Program, 2021). Ground-based remote sensing observations with SO_2 camera during fieldwork 2016 and 2019 found emissions close to detection limit (<< 100 t per day).

Renewed deformation with uplift of up to 39 mm/month and increased seismicity was detected at Rabaul from September 2021 onwards (Global Volcanism Program, 2021). The ongoing uplift resulted in a cumulative vertical displacement of ~7 cm until November 2024. Additionally, fumarolic activity produced white emissions of ~90–150 C (McCormick Kilbride et al., 2024), but no further signs for volcanic activity were detected at Rabaul (Global Volcanism Program, 2024).

2.3 Previous work on Rabaul volcanic outgassing and melt inclusions

So far, two studies have analysed volatiles in melt inclusions at Rabaul (Bouvet de Maisonneuve et al., 2015; Roggensack et al., 1996). Olivine-hosted basaltic melt inclusions from the 1994 eruption of Tavurvur contain 2.8–3.8 wt% H_2O and up to 960 ppm CO_2, whereas plagioclase-hosted dacitic melt inclusions from the 1994 eruption of Vulcan contain 2.0–2.3 wt% H_2O and <50 ppm CO_2, indicating extensive CO_2 outgassing prior to inclusion trapping

(Roggensack et al., 1996). Pyroxene- and plagioclase hosted melt inclusions from the 2006 eruption of Tavurvur are compositionally similar to those of the 1994 Tavurvur eruption, and contain ~2.5 wt% H_2O and 400–500 ppm CO_2 (Bouvet de Maisonneuve et al., 2015).

Mafic magmas from the 2006 Tavurvur eruption contain up to 4000 ppm SO_2 (Bouvet de Maisonneuve et al., 2015). Melt inclusion SO_2 contents decrease with increasing SiO_2, which may reflect crystallisation under volatile-saturated conditions (Bouvet de Maisonneuve et al., 2015). SO_2 emissions during the 2006 eruption were measured by OMI satellite (230 kt, Carn et al., 2009) and correspond closely to the magmatic SO_2 budget calculated from melt inclusion and eruption volume data (240–640 kt, Bouvet de Maisonneuve et al., 2015). Bouvet de Maisonneuve et al. (2015) concluded that this eruption was not triggered by overpressurization of the magma reservoir through accumulation of a co-magmatic volatile phase in the plumbing system. Whether this is true for other eruptions is unknown and has major implications for the style and intensity of future eruptions at Rabaul.

3. Analytical methods

3.1 Sampling

The samples analysed in this study were previously investigated by Höhn et al. (2026). Volcanic bombs (VB_IA, VB_IB) were collected from two sites on the northern flank and environs of the Tavurvur cone in September 2016 (4S 13.815', 152E, 12.205'). Volcanic bombs at Tavurvur are dark grey in colour and vary in size from ~50 cm to ~3 m, though many of the larger bombs have been broken up and removed by local people. For this study, we collected fist-sized pieces. The collection of bombs with minimal alteration was prioritised. The bombs show abundant macrocrysts (defined as crystals isolated in the matrix with size 0.5–2 mm) as

well as mineral clots (defined as aggregates of two or more crystals) which are visible to the naked eye. They are embedded in a glassy groundmass. There was no clear difference between bomb morphology, colour, vesicularity or mineralogy between the two sites. Both of these two volcanic bombs have been previously analysed for their whole rock compositions; they are basaltic andesites (Fig. 2) (Höhn et al., 2026). Sample VB_IA contains 56.3 wt% SiO_2, 8.0 wt% CaO, and 4.2 wt% MgO, while sample VB_IB contains 56.9 wt% SiO_2, 7.9 wt% CaO, and 4.0 wt% MgO. These compositions place them at the more primitive end of the spectrum of eruption products from the 2014 event, which range from basaltic andesite to dacite, with SiO_2 contents between 56.7 and 63.4 wt% (Fabbro et al., 2020).

3.2 Sample processing

We crushed three fist-sized pieces of each volcanic bomb sample in a stainless steel mortar. To preserve the textural context of the crystals, we separated small sample pieces containing only macrocrysts from small pieces containing only mineral clots and further crushed these pieces into individual crystals. We handpicked these crystals according to type (plagioclase or mafic mineral) and textural context (macrocryst or mineral clot) using a binocular microscope. Picked crystals were mounted individually on small glass plates using CrystalBond™ and polished to expose glassy melt inclusions at the surface. Crystals with exposed melt inclusions were then mounted in 1-inch epoxy rounds and re-polished to ensure a flat surface for microanalysis.

3.3 Secondary Ion Mass Spectrometry (SIMS)

We carried out secondary ion mass spectrometry (SIMS) measurements in October 2022 using the Camera ims 7f-GEO instrument at the NERC Ion Microprobe Facility, University of Edinburgh, UK. SIMS measurements were conducted before any conductive carbon coating

was applied to the samples, to ensure the fidelity of CO_2 measurements. We measured H_2O, CO_2, F and selected trace elements (Sr, Y, Zr, Nb, Ba, La, Ce, Nd, Sm, Eu, Gd, Dy, Yb, Th) in 87 naturally quenched, glassy plagioclase-, clinopyroxene-, and olivine-hosted melt inclusions and matrix glasses. Detailed information on the instrument set-up and analytical conditions can be found in Supplementary File S1. Volatile and trace element data for the 2014 melt inclusions can be found in Supplementary File S2.

3.4 Micro-Raman Spectroscopy

Thirty-nine melt inclusions contained at least one bubble while 63 MIs were bubble free. The bubbles were found in plagioclase- (n=20), clinopyroxene- (n=8), and olivine-hosted (n=16) melt inclusions. They occupy volumes between 0.02 and 8.71 vol% of the melt inclusions. The volume of the melt inclusions was calculated assuming ellipsoidal shape. Bubbles can be trapped as a free fluid phase but more commonly form when post-entrapment crystallisation within an inclusion causes CO_2 to be released from the melt (Aster et al., 2016; Venugopal et al., 2020b). We were unable to conduct Raman spectroscopy on 32 bubbles that were breached during sample preparation, so the reported CO_2 contents for these inclusions are glass-only and should be considered as minima. Raman spectroscopy on five unbreached bubbles revealed no Fermi diads suggesting that the bubbles were CO_2-free or contain very low concentrations of CO_2 beneath the detection limit. For the two bubbles that did contain measurable CO_2, we added this to the glass to obtain the total CO_2 concentration. The bubble in melt inclusion M10_05.03 contains 53% of the total CO_2 in the MI, while the bubble in melt inclusion M11_06.10_02.1 contains 75% of the total CO_2. We also conducted Raman spectroscopy on a further five unbreached bubbles in MIs that were not analysed by SIMS and found no Fermi diads for any of these bubbles and detected no CO_2 in them. Detailed information on the Raman

spectroscopy and CO_2 calculations can be found in Supplementary File S1.

3.5 Electron Probe Microanalysis (EPMA)

We measured major and minor elements, SO_2, and Cl in the melt inclusions, their host minerals, and matrix glasses by electron microprobe (EPMA) at the Department of Mineralogy, University of Münster, Germany. Analysis conditions were set at 15 kV accelerating voltage and 20 nA beam current for melt inclusions and matrix glasses and 15 kV and 15 nA for host minerals. The counting times on peak and background positions were varied according to element concentration: from 5 s on peak for major elements to 120 s on peak for trace elements. Backgrounds on both sides of the peak were measured for half of the peak time. The beam diameter was set to 3–8 μm for melt inclusions and matrix glasses depending on available space. The beam diameter for host minerals was set at 10 μm. Detailed information on the analytical conditions and precision and accuracy for EPMA analysis can be found in Supplementary File S1. All EPMA data can be found in Supplementary Files S2 and S3.

3.6 Ozone Monitoring Instrument, Infrared Atmospheric Sounding Interferometer, and PlumeTraj

The Ozone Monitoring Instrument (OMI) is a hyperspectral UV-visible solar backscatter spectrometer that was deployed aboard NASA's Aura satellite, launched in July 2004 (Levelt et al., 2006). The satellite flies in a sun-synchronous polar orbit, crossing the Equator at 13:45 local time (ascending node) at an altitude of 705 km. The instrument's design incorporates a relatively high spatial resolution and a wide swath, enabling it to provide continuous daily global coverage. The swath is binned into pixels measuring 24×13 km at nadir and significantly more, up to 26×150 km at swath edge. Operating primarily in the UV and visible

portions of the electromagnetic spectrum, OMI measures the solar radiation that is scattered back from the Earth's atmosphere and surface. Its primary objective is to monitor the spatial and temporal distribution of ozone. In addition, OMI also detects other trace gases such as NO_2, SO_2, and HCHO, as well as aerosol properties and cloud parameters (Levelt et al., 2006). Global OMI observations of volcanoes have been valuable in detecting and quantifying SO_2 emissions from both eruptions (Carn et al., 2008; McCormick et al., 2015, Carn et al., 2016) and persistent degassing (Carn et al., 2008; McCormick et al., 2012; McCormick et al., 2014, Carn et al., 2017). In this work, we used version 2.0 of the OMI SO_2 retrieval algorithm (Li et al., 2020).

The Infrared Atmospheric Sounding Interferometer (IASI) is an infrared sounder that operates aboard the MetOp A, B, and C satellites, which were launched in 2006, 2012, and 2018, respectively. In contrast to OMI, IASI uses Fourier Transform Spectroscopy to measure the infrared radiation emitted from the Earth and its atmosphere. The satellites are in a polar orbit, each separated by 50 minutes and achieve near-global coverage every 12 hours. Each scan has a swath width of 2,200 km composed of four circular pixels with a diameter of 12 km at nadir within a 50 km by 50 km nadir (Clerbaux et al., 2009). IASI measurements span the spectral range of 645 to 2760 cm^{-1}, which includes all three SO_2 absorption features in the infrared. A number of methods have been developed to extract information about SO_2 from the IASI spectra. (e.g. Clarisse et al., 2008; Walker et al., 2011; Carboni et al., 2012; Clarisse et al., 2012; Walker et al., 2012, Clarisse et al., 2014). In this study the Walker et al. (2011, 2012) linear retrieval is used for detecting pixels with elevated levels of SO_2, and the Carboni et al. (2012, 2018) iterative retrieval scheme is used for quantification of SO_2 amount and height.

We used the PlumeTraj toolkit to calculate the mass of SO_2 erupted during the 2014 eruption from both the OMI and IASI data (Pardini et al., 2018; Queisser et al., 2019; Burton et al., 2021; Esse et al., 2023; Hayer et al., 2023). We implement the forward version of PlumeTraj which determines the time and altitude of injection of each satellite pixel by calculating possible atmospheric trajectories from a range of altitudes above the vent throughout the eruption (Esse et al. 2025a, Esse et al. 2025b). For this, the SO_2satellite data is combined with the Hybrid Single Particle Lagrangian Integrated Trajectory (HYSPLIT) model of the National Oceanic and Atmospheric Administration's (NOAA) (Cohen et al., 2015) in the PlumeTraj toolkit. The routes of these trajectories diverge due to wind shear in the atmosphere so that only those at potential plume altitudes arrive at the pixel location at the time of satellite overpass. The entire sub-day emission history can then be reconstructed from the satellite SO_2image by using the injection time and altitude as the time and altitude of closest approach to the vent.

To select which pixels are used for PlumeTraj analysis we applied thresholding to the satellite data as follows. For OMI, all pixels that had a VCD greater than 0.1 DU and were larger than the reported noise were selected. For IASI, all values that were above the reported error were used. Additionally, the IASI data was resampled onto a regular latitude-longitude grid with a spacing of 0.5°.

One important factor is the height-sensitivity of both satellite instruments to SO_2, which decreases the lower the plume in the atmosphere. To account for this, all OMI SO_2 columns are corrected to the plume altitude by linearly interpolating between the available VCD values (at 0.9, 2.5, 7.5 and 17 km above sea level). For IASI, the height corrected VCD value provided by the iterative retrieval is used.

4. Results

4.1 Petrography and mineral assemblage

Thin sections of the 2014 samples reveal a porphyritic texture with a brown, fine-grained, glassy matrix (~60 vol%) containing microcrystalline plagioclase needles and small pyroxene crystals interspersed throughout. The general mineral assemblage consists of plagioclase (~30 vol%), clinopyroxene (~6 vol%), orthopyroxene (~2 vol%), olivine (~1 vol%) and Ti-magnetite (~1 vol%) as well as accessory apatite and sulphides. Fewer than ten mineral clots were counted in each thin section making them less common than macrocrysts in terms of area covered (Fig. 3, Supplementary Fig. S3). A detailed discussion of the petrology and texture of the Rabaul eruption products including mineral textures and chemistries can be found in Höhn et al. (2026).

4.2 Melt inclusion host minerals

Plagioclase

Plagioclase crystals hosting melt inclusions have anorthite (An) contents (An = molar $CaO/(CaO+Na_2O+K_2O)$) between 62 and 93 mol% with peaks at An_{70}, An_{83}, and An_{93} (Fig. 4). Höhn et al. (2026) extensively analysed the mineral chemistry of products from different eruptions at Rabaul, including the volcanic bombs from the 2014 eruption of Tavurvur, and classified plagioclase crystals into three groups based on mineral chemistry and zoning patterns. Group one plagioclase crystals have cores with $An_{91–97}$ (An_{93} is most common, Fig. 4) and are normally zoned with rims of $An_{<75}$ (Fig. 3a). Group two plagioclase crystals have heavily resorbed cores with $An_{80–89}$ (An_{82} most common, Fig. 4) and rims of $An_{<75}$ (Fig. 3b). The third group of plagioclase crystals display either no zoning or faint oscillatory zoning and

these crystals have $An_{<75}$, with the most frequent composition being An_{69} (Figs. 3c, 4) (Höhn et al., 2026).

Most of the plagioclase host crystals analysed in this study (n=44) are group three plagioclase, two are classified as group two (M09_06.01 and M9_06.09) and one crystal is classified as group one (M10_03.07). However, these three plagioclase crystals have interconnected systems of melt inclusions in a pattern which is consistent with formation during dissolution and recrystallisation of the crystal (Supplementary Fig. S4). Therefore, the melt inclusions in these minerals are not primary melt inclusions that were trapped during original crystallisation, but instead are secondary inclusions trapped during the recrystallisation stage. We are therefore only considering the group three plagioclase host minerals in all further discussions.

Clinopyroxene

Clinopyroxene melt inclusion host minerals show a bimodal Mg# (Mg# = molar MgO/(MgO+FeO)) distribution ranging from Mg#62 to Mg#93 with peaks at Mg#76 and Mg#83 (Fig. 4). According to Höhn et al. (2026), clinopyroxene crystals in Rabaul eruption products can be distinguished into two groups based on their texture and mineral composition. Group one clinopyroxene crystals are predominantly diopsidic ($Wo_{47}En_{46}Fs_{7}$) with core compositions of ~Mg#>84 and rims of ~Mg#75 (Figs. 3e, 4). In contrast, group two clinopyroxene crystals are predominantly augitic ($Wo_{42}En_{44}Fs_{13}$) with cores of ~Mg#75 (Fig. 4). These crystals are unzoned or exhibit only faint oscillatory zoning (Fig. 43) (Höhn et al., 2026). From the 16 clinopyroxene host minerals of the 2014 melt inclusions, seven crystals can be classified as group one clinopyroxene and nine as group two clinopyroxene (Fig. 4).

Olivine

Olivine crystals hosting melt inclusion have (Fo) contents (Fo = molar MgO/(MgO+FeO)) ranging from 69 mol% to 84 mol%. Most crystals (n=21) have cores with $Fo_{77–84}$ (Fo_{80} most common, Fig. 4), we only found three crystals with $Fo_{69–70}$. Olivine crystals in thin sections from the 2014 volcanic bombs have core compositions of $Fo_{77–84}$ with Fo_{81} being most common (Fig. 4) (Höhn et al., 2026).

4.4 Melt inclusion and matrix glass chemistry

Major and Trace Elements

Melt inclusions in the 2014 volcanic bombs are found within group three plagioclase, group one and group two clinopyroxene, and olivine, occurring in both mineral clots and macrocrysts (Fig. 6). The melt inclusions are predominantly round or slightly elongated, with sizes between around 20 and 300 μm. The melt inclusions record SiO_2 contents between 46.2 and 69.5 wt%, MgO between 0.8 and 6.0 wt%, CaO between 2.2 and 13.8 wt%, and FeO between 3.2 and 13.4 wt%.

We corrected the melt inclusion data for post entrapment crystallisation (PEC), which describes crystallisation of the host mineral at the host-inclusion interface during cooling or decompression of the system (Roedder, 1984; Frezzotti, 2001). Corrections were carried out for all melt inclusions by adding the host mineral composition incrementally back into the melt inclusion until the equilibrium K_D value between melt and mineral was reached. Detailed information on the PEC correction methods for the 2014 melt inclusions can be found in the supplementary materials. The correction values for plagioclase-, clinopyroxene- and olivine-hosted melt inclusions are 0.0 to 23.5% (mean = 8.9), -6.4 to +8.2% (mean = 0.1) and -2.5 to

+5.0% (mean = 3.0) respectively. Negative PEC values (n=11 melt inclusions) indicate that some melt inclusions experienced dissolution of the host mineral into the melt phase prior to eruption. All further discussion of melt inclusion compositions will be for PEC-corrected values.

After PEC corrections, melt inclusion SiO_2 contents are between 46.9 and 66.2 wt%, MgO between 0.6 and 6.2 wt%, CaO between 3.9 and 15.1 wt%, and FeO between 2.8 and 12.0 wt% which means that they have basaltic to dacitic compositions (Figs. 6, 7a–d). There is substantial variation in the melt inclusion chemistries as a function of host mineral. Olivine-hosted melt inclusions are the most primitive with MgO contents ranging from 3–6 wt%, while group three plagioclase-hosted melt inclusions are the most evolved with MgO ranging from 0.5–1.5 wt%. Melt inclusions in group one clinopyroxene have distinctly different chemical compositions from melt inclusions in group two clinopyroxene. Melt inclusions in group one clinopyroxene have MgO contents between 3.5 wt% and 5.5 wt% and show similar major element compositions, for example CaO or K_2O, to melt inclusions hosted in olivine (Fig. 7a, d). In contrast, melt inclusions in group two clinopyroxene have MgO concentrations between 2 wt% and 3 wt% and show element compositions that are more similar to melt inclusions hosted in group three plagioclase than melt inclusions in olivine (Figs. 7, Supplementary Figs. S3, S4).

Melt inclusions in olivine and group one clinopyroxene display clear positive correlations of increasing MgO content with selected incompatible trace elements as shown in Fig. 8e–h, while melt inclusions in group three plagioclase and group two clinopyroxene show a wider range of trace element concentrations over a narrower range in MgO. The trace elements Nb, Ce, Dy and Nd were selected due to their frequent use as indicators of volatile abundance, given their comparable behaviour in terms of incompatibility to certain volatiles during mantle melting

and fractional crystallisation. Specifically, Ce is often used as a proxy for H_2O, Nb for CO_2, Dy for S, and Nd for F (Michael, 1995; Saal et al., 2002; Ruscitto et al., 2012; Muth and Wallace, 2022).

We modelled fractional crystallization using the software Petrolog3 (Danyushevsky and Plechov, 2011). We used the forward crystallization model to calculate liquid lines of descent (LLD) using the three most primitive melt inclusions as starting compositions (M11_06.02, M09_07.12_01.2, M09_08.04) as well as the mean composition of the four most primitive melt inclusions. Crystallisation was permitted for olivine, plagioclase, clinopyroxene and magnetite. Calculations were carried out using the mineral-melt equilibrium models of Danyushevsky (2001) for olivine, plagioclase, and clinopyroxene in one run and the models of Langmuir et al. (1992) for olivine, plagioclase, and clinopyroxene in a second run. In both runs the mineral-melt equilibrium model of Ariskin and Barmina (1999) was used for magnetite. Calculations were carried out at 2 kbar with an oxygen buffer of ΔQFM+1. The selection of pressure and oxygen buffer are based on thermobarometry and oxybarometry calculations for the Rabaul eruption products by Höhn et al. (2026). Trace elements were modelled using the mineral-melt partition coefficients for basaltic liquids from Rollinson and Pease (2021).

Figure 8 and Supplementary Figures S3, and S4 show the overall best fitting LLDs which were calculated with melt inclusion M11_06.02 as the starting composition. The olivine- and group one clinopyroxene-hosted melt inclusions follow the fractional crystallisation trends fairly closely, especially for trace elements (Fig. 7e–h, Supplementary Fig. S4). Deviations from the fractional crystallisation trend for major elements can be explained by post-entrapment crystallisation, especially for MgO and FeO which are most affected by PEC (Roedder, 1984). In contrast, most of the group three plagioclase- and group two clinopyroxene-hosted melt

inclusions deviate from the fractional crystallisation trend, especially in the trace elements (Fig. 7e–h, Supplementary Fig. S4).

Major and minor elements in matrix glasses in the 2014 volcanic bombs have been previously analysed by Höhn et al. (2026). The matrix glasses show a narrow chemical composition in SiO_2 (58.1–62.3 wt%) and vary in Al_2O_3 between 12.8 and 22.4 wt%, with MgO values ranging from 1.0–5.0 wt%, FeO from 3.8–8.7 wt% and CaO between 4.6 and 8.4 wt%. Most matrix glasses overlap in their major elements with those of group three plagioclase- and group two clinopyroxene-hosted melt inclusions while a small group of matrix glasses overlap in their major elements with those shown by olivine- and group one clinopyroxene-hosted melt inclusions (Fig. 7a–d, Supplementary Fig. S3). Trace element concentrations in the matrix glasses are varied but mostly similar to those in group three plagioclase- and group two clinopyroxene-hosted melt inclusions (Fig. 7e–h, Supplementary Fig. S4).

4.5 Volatiles

H_2O

H_2O concentrations in olivine-hosted melt inclusions are higher (2.3 ±0.5 wt%) than in melt inclusions in group three plagioclase hosts (0.9 ±0.5 wt%). Melt inclusions in group one clinopyroxene have H_2O concentrations between 2.1 and 3.0 wt% overlapping with those of olivine-hosted melt inclusions, while melt inclusions in group two clinopyroxene show H_2O contents between 0.2 and 1.8 wt% which are similar to those in plagioclase-hosted melt inclusions (Fig. 9a). Matrix glasses are heavily degassed with low H_2O contents (0.10 to 0.15 wt%). Olivine-hosted melt inclusions show a trend of constant H_2O with increasing Ce, while clinopyroxene-hosted melt inclusions exhibit decreasing H_2O concentrations with increasing

Ce (Fig. 8a) which in both cases results in decreasing H_2O/Ce ratios with increasing K_2O (Fig. 8b). Group three plagioclase-hosted melt inclusions show no distinct trends in a diagram of H_2O vs. Ce but have overall low H_2O and high Ce concentrations and therefore low H_2O/Ce ratios.

SO_2

Similar to H_2O, SO_2 concentrations in olivine-hosted melt inclusions are higher (2630 ±930 ppm) than in melt inclusions in group three plagioclase hosts (670 ±290 ppm) (Fig. 8c). Clinopyroxene-hosted melt inclusions display a wide range in SO_2 contents with 2500–4700 ppm in group one clinopyroxene and 540–2600 ppm in group two clinopyroxene crystals. Both olivine-and group one clinopyroxene-hosted melt inclusions show decreasing SO_2 concentrations with increasing Dy and consequently decreasing S/Dy ratios with increasing K_2O (Figs. 8c–d). Analyses of group three plagioclase- and group two clinopyroxene-hosted melt inclusions yield a range of Dy concentrations over a narrow range of SO_2 and no trends in S/Dy space. Matrix glasses are very SO_2 poor (40–174 ppm).

CO_2

Bubbles in melt inclusions may form because of changing volatile solubility within the melt inclusions as a result of changing melt composition during post-entrapment crystallisation or decompression during magma ascent (Maclennan, 2017). These bubbles tend to sequester volatiles, especially CO_2, resulting in an underestimation of the total volatile content when only the glass is analysed (Moore et al., 2015; Maclennan, 2017; Venugopal et al., 2020b). Most bubbles in the 2014 melt inclusions show a linear relationship between bubble volume and melt inclusion volume with typical bubble volume proportions ranging from 0.02 to 1.16 % (Supplementary Fig. S2). The small and near-uniform volume proportion occupied by the bubble suggests that these melt inclusions only trapped melt and that the bubbles were

generated in the melt inclusions after trapping (Moore et al., 2015). However, several melt inclusions contain bubbles with higher volume percentages of up to 8.7% which deviate from the linear trend. These bubbles might contain a free fluid phase and could indicate heterogeneous trapping of a mixed melt-fluid phase (e.g. Steele-MacInnis et al., 2017).
Raman analyses showed that a number of bubbles within the linear trend are CO_2-free. While we cannot exclude that some of the melt inclusions which contained breached bubbles might have contained CO_2, our investigation suggests that most of the bubbles in the 2014 melt inclusions are small and empty and are most likely true shrinkage bubbles.

While most melt inclusions have CO_2 contents below 600 ppm, a subset of four melt inclusions in group three plagioclase and one melt inclusion in olivine show the highest CO_2 concentrations among all analysed melt inclusions, ranging from 802 to 1026 ppm (Fig. 8e). The remaining plagioclase-, olivine- and clinopyroxene-hosted melt inclusions display CO_2 values from 8 to 384 ppm, 4 to 347 ppm, and 2 to 622 ppm, respectively. Most melt inclusions show a steep decline in CO_2 with increasing Nb (Fig. 8g). The CO_2/Nb ratios are therefore also rapidly decreasing with increasing K_2O (Fig. 8h). CO_2/Nb ratios are relatively low for all analyses (CO_2/Nb = 2–654) except for MI11_06.10_02.1. This melt inclusion analysis yielded 1001 ppm of CO_2 and 0.48 ppm of Nb, giving it a CO_2/Nb ratio of 2082 which is by far the highest ratio of all of the analysed melt inclusions. No correlation can be observed between CO_2 and H_2O (Fig. 8g). Matrix glasses contain very little CO_2 and are considered to be fully degassed.

Halogens (Cl and F)

Cl and F concentrations increase with increasing K_2O and Nd for olivine- and clinopyroxene-hosted melt inclusions from 0.06 to 0.35 wt% Cl and 61 to 905 ppm F (Fig. 9a, c). However,

both Cl and F show a sharp drop in plagioclase-hosted melt inclusions and therefore also a rapid decline of Cl/K and F/Nd ratios with increasing K_2O (Fig. 9b, d). This sharp drop in Cl and F concentrations could be the result of late-stage apatite crystallisation. Melt inclusions in olivine and group one clinopyroxene display a general trend of decreasing Cl/K and increasing F/Nd ratios with increasing K_2O contents (Fig. 9b, d). Matrix glasses have Cl concentrations of 0.13 to 0.21 wt% and variable F contents of 23 to 415 ppm.

4.6 The SO_2 budget of the 2014 Rabaul eruption

We calculated the SO_2 budget of the 2014 eruption of Tavurvur with two different methods. First, we used OMI and IASI satellite observations of the SO_2 emissions injected into the atmosphere over Rabaul and the PlumeTraj toolkit to calculate SO_2 emissions as a function of time and altitude, in order to obtain a total SO_2 mass loading of the eruption. Secondly, we use the melt inclusion data to calculate the SO_2 budget from the petrological record, calculating the erupted mass of magma by the use of estimated eruption source parameters (plume altitude, mass eruption rate, eruption duration). Both methods are described below.

Calculation of the SO_2 budget from satellite observations

The OMI overpass on the 29 August occurred at ~13:00 local time, 9.5 hours after the eruption had started (Supplementary Fig. S5b, c). The eruption cloud can be seen extending westwards across the New Britain region. Unfortunately, the SO_2 plume is situated right on the edge of the OMI swath. At these extreme satellite viewing angles, the large pixel size in the field of view introduces substantial uncertainties into PlumeTraj results, as the tool was designed to use TROPOMI data which has a much higher spatial resolution (Esse et al., 2023). The subsequent OMI overpass on the 30 August (at 13:34–13:40 local time, ~34 hours after the

eruption had started) has an improved view of the eruption plume, now lying towards the centre of the swath. However, by late 2014 the OMI swath was substantially influenced by the so-called OMI row anomaly, a persistent data gap in the swath centre attributed to a partial blockage of the instrument's viewing port (Torres et al., 2018). As a result, part of the SO_2 plume is missing from the satellite image (Fig. 10a). Any quantification of SO_2 emissions based on the OMI imagery, therefore represents a minimum estimate.

IASI satellite observations from the 29 August to 31 August are not affected by data gaps and permit imaging of the whole SO_2 emission plume which allows us to assess the geometry of the plume from the 2014 eruption of Tavurvur as it disperses and estimate the areal extent of the plume missing from the OMI imagery (Figs. 10c, 10e, Supplementary Fig. S5). However, the low SO_2 column amount associated with the 2014 eruption of Tavurvur introduces substantial uncertainties into the Carboni (2012) SO_2 retrievals. We have therefore used both IASI images (29 and 30 August), and the OMI image on 30 August, as inputs in PlumeTraj to calculate three estimates of the SO_2 budget.

The PlumeTraj derived SO_2 emission time series for the OMI overpass of 30 August is shown in Figure 10b. The calculated injection time of SO_2 is between 16:00 on 28 August and 16:00 on 29 August with the bulk of the SO_2 emission taking place between ~19:00 on 28 August and ~04:00 on 29 August (local time). The peak value is ~1500 kg/s and the highest altitude retrieved is 10 km. The total SO_2 mass, obtained by integrating under the curve is 17.1 ±2.7 kt. Our estimate of peak altitude is somewhat lower than the 18 km reported in contemporary GVP reports (Global Volcanism Program, 2014; Global Volcanism Program, 2017). Various sources are cited for the 18 km estimate, from satellite observations and airline pilot observations to alerts issued by the Darwin Volcanic Ash Advisory Centre. We note that pilot

and ground-based reports and satellite observations can have significant discrepancies (Tupper and Wunderman, 2009) and the reasons for these mismatches remain unclear. Our PlumeTraj calculations place the peak SO_2 emissions before the reported eruption start time. This directly contradicts eyewitness statements who did not report major emissions from Tavurvur before the eruption started at ~04:00 local time on 29 August (Global Volcanism Program, 2014). This time shift corresponds to a roughly 10% error on injection time in PlumeTraj, which we attribute to the fact that the trajectories are being run over ~34 hours. As these errors are likely to be systematic in nature, the time evolution of the emissions is expected to still be reliable even though the exact timings may be shifted.

The PlumeTraj derived SO_2 emission time series for the IASI overpasses of 29 August are shown in Figure 10d. The calculated injection time of SO_2 is between 06:00 on 29 August and 10:00 on 30 August with the bulk of the SO_2 emission taking place between ~18:00 on 29 August and ~10:00 on 30 August (local time). The peak value is ~600 kg/s and the highest altitude retrieved is ~16 km. The total SO_2 mass, obtained by integrating under the curve is 19 ±4 kt. The PlumeTraj derived SO_2 emission time series for the IASI overpasses of 30 August are shown in Figure 10f. The calculated injection time of SO_2 is between 10:00 on 29 August and 14:00 on the 30 August with the bulk of the SO_2 emission taking place between ~18:00 on 29 August and ~10:00 on 30 August (local time). The peak value is ~900 kg/s and the highest altitude retrieved is ~16 km. The total SO_2 mass, obtained by integrating under the curve is 18 ±7 kt. For both IASI derived SO_2 emission time series PlumeTraj calculations are placing the peak SO_2 emissions after the reported eruption start time with a time shift of roughly 12 hours, which we again attribute to the fact that the trajectories are being run over ~34 hours.

Both the IASI and the OMI derived SO_2 budgets agree with each other within uncertainty. Our

calculated SO_2 budgets match with an SO_2 emission estimate made by S. Carn (~18.5 kt, OMI satellite, Global Volcanism Program, 2014). The IASI derived PlumeTraj calculations yield SO_2 budgets (19 ±4 kt and 18 ±7 kt) for the 2014 eruption of Tavurvur that are at most ~10% higher than the result from the OMI derived PlumeTraj calculations (17.1 ±2.7 kt) taking uncertainties into account. We therefore conclude that the OMI data from the overpass on the 30 August caught the main body of the SO_2 plume with only the margins of the plume missing from the image.

Calculation of the SO_2 budget from the petrological record

We used melt inclusions in volcanic bombs to calculate the SO_2 budget during the 2014 eruption with the petrological method. Since there are no estimates for the erupted volume during the 2014 eruption, we used estimates for the plume height to calculate the peak mass eruption rate, which we used together with the estimated duration of the eruption and the SO_2 content of the melt inclusions and matrix glass to calculate the mass of erupted SO_2.

In a first step, we estimated the peak mass eruption rate (peak MER) using the plume height-mass flux model of Mastin et al. (2009) with H_{obs} being the height above the went in km:

$$peak\ MER = 140\ H_{obs}^{4.15} \quad (1)$$

For this, we need the plume height of the 2014 eruption which was stated to be ~18 km high in a bulletin report of the global volcanism program (Global Volcanism Program, 2014). However, our OMI derived SO_2 emission time series shows a main SO_2 injection altitude of ~10 km (Fig. 10b), while the IASI derived SO_2 emission time series show another smaller SO_2 plume at an altitude of ~14 km (Figs. 10d, 10f). Using Equation (1), we calculate a mass

eruption rate of 2.0 x 10^6 kgs^{-1} for the 2014 Tavurvur eruption using a plume height of 10 km and a mass eruption rate of 8.0 x 10^6 kgs^{-1} using a plume height of 14 km (Table 1).

Next, we calculated the total mass of erupted magma (M_{magma} in kg) by multiplying the peak mass eruption rate (peak MER in kgs^{-1}) with the duration of the eruption (t in seconds):

$$M_{magma} = peak\ MER \times t \quad (2)$$

The 2014 eruption started shortly after 03:30 local time on the 29 August 2014 and died down after 06:40 on 30 August (Global Volcanism Program, 2014). According to the 2014 bulletin report of the global volcanism program, the first strombolian explosion lasted until 06:57 on 29 August, but was followed by further, albeit smaller, explosions until 06:40 on 30 August. We can deduce the main phase of SO_2 injection from our PlumeTraj models, which give an injection duration of ~8 hours, equalling 28800 s for the OMI derived SO_2 emission time series (Fig. 10b) and an injection duration of ~12 hours, equalling 43200 s for the IASI derived SO_2 emission time series (Figs. 10d, 10f). We therefore calculate a total mass of erupted magma of 5.7 x 10^{10} kg for a plume height of 10 km and an eruption duration of 8 hours (parameters from the OMI derived SO_2 emission time series) and a total mass of erupted magma of 3.5 x 10^{11} kg for a plume height of 14 km and an eruption duration of 12 hours (parameter from the IASI derived SO_2 emission time series).

We calculate the mass of the erupted melt (M_{melt}) by multiplying the total mass of magma with the estimated crystallinity of the melt. We estimate the crystallinity to be 0.38 based on the estimated volume percentage of matrix glass, minerals and vesicles in the 2014 volcanic bombs (Höhn et al., 2026). Altogether, we calculate a mass of the erupted melt of 3.5 x 10^{10} kg for a

plume height of 10 km and an eruption duration of 8 hours and a mass of erupted melt of 2.1 x 10^{11} kg for a plume height of 14 km and an eruption duration of 12 hours (Table 1).

In the last step, we multiply the calculated mass of the melt with the difference of the SO_2 in the melt inclusions and the SO_2 in the matrix to get the mass of SO_2 released during the eruption:

$$M_{SO2} = M_{melt} \text{ x } (SO2_{MI} - SO2_{matrix}) \quad (3)$$

Figure 11 shows a kernel-density diagram of the SO_2 concentrations in the melt inclusions divided into the different host minerals. The diagram shows a range of SO_2 concentrations with a peak at the upper end of 6000 ppm SO_2 in the olivine-hosted melt inclusions and a peak at the lower end of 700 ppm SO_2 in plagioclase-hosted melt inclusions.

Analyses of the melt inclusions reveal a rapid decline of SO_2 with increasing Dy, particularly in those hosted in olivine and group one clinopyroxene. This trend suggests that significant degassing of sulfur occurred during the crystallisation of these minerals (Fig. 8c). In contrast, melt inclusions entrapped in group three plagioclase and group two clinopyroxene exhibit consistently lower SO_2 contents, recording a more degassed state of the melt with little residual sulfur available to correlate with Dy. Moreover, the major element chemistry of the melt inclusions suggests the involvement of different magmas in this eruption – a relatively mafic

and volatile-rich end-member, represented by the olivine- and group one clinopyroxene-hosted melt inclusions, and a more evolved and volatile-poor composition represented by the group two clinopyroxene- and plagioclase-hosted melt inclusions. Although the mafic magma, plausibly akin to the recharge melts that have triggered historical eruptions at Tavurvur (Höhn et al., 2026) exhibits higher volatile contents, it constitutes only a minor proportion of the

overall volume of the magmatic system and the material erupted, based on the basaltic-andesitic whole rock composition of the 2014 volcanic bombs (Höhn et al., 2026). Consequently, we consider the SO_2 budget derived from the group three plagioclase-hosted melt inclusions a more reliable indicator of the volatile content relevant to the 2014 eruption.

We therefore conducted out SO_2 budget calculations with an SO_2 melt inclusion content of 700 ppm and the average amount of SO_2 measured in the matrix glass (112 ppm). Our calculations yield a mass of erupted SO_2 of 21 kt for a plume height of 10 km and eruption duration of 8 hours and a mass of erupted SO_2 of 130 kt for a plume height of 14 km and eruption duration of 12 hours (Fig. 12). Both the plume height and the SO_2 melt inclusion concentration have the biggest influence on the uncertainty of the SO_2 budget results. Changing the plume height by 1 km changes the SO_2 budget by 50%, while changing the SO_2 melt inclusion concentration by 500 ppm changes the SO_2 budget by 85%.

5. Discussion

5.1 Melt inclusions capture two different magmas

Recent modelling indicates that the products of the post-Rabaul Pyroclastics eruptions were generated by the mixing of two distinct magmas: a basaltic magma, comparable to the basaltic enclaves of the 1937 eruption, and a dacitic magma whose composition is similar to that of the average Rabaul Pyroclastics eruption products (Bernard and Bouvet de Maisonneuve, 2020; Fabbro et al., 2020; Höhn et al., 2026). The basaltic magma represents the mafic recharge magma which fuels volcanism at Rabaul and is identified by the presence of distinctly mafic minerals, such as olivine, group one plagioclase, and group one clinopyroxene which crystallised from the mafic recharge magma and were transferred into the carrier liquid during

mixing with the more dacitic magma (Patia, 2004; Bouvet de Maisonneuve et al., 2015; Patia et al., 2017; Bernard and Bouvet de Maisonneuve, 2020; Fabbro et al., 2020; Höhn et al., 2026). In contrast, group three plagioclase and group two clinopyroxene are interpreted to have crystallised from the evolved, dacitic magma (Höhn et al., 2026).

Melt inclusions hosted within the 2014 volcanic bombs again capture evidence of both the basaltic and dacitic magmatic components. Their trace element and volatile compositions, which remain largely unaffected by post-entrapment crystallisation, reveal that inclusions in olivine and group one clinopyroxene possess similar, relatively primitive compositions and higher volatile contents compared to those in group three plagioclase and group two clinopyroxene. The inclusions in olivine and group one clinopyroxene follow a fractional crystallisation trend (Fig. 7, Supplementary Figs. S3, S4), whereas those hosted in group three plagioclase and group two clinopyroxene deviate from this trend, indicating that they cannot have formed by the same fractional crystallisation trend as the olivine- and group one clinopyroxene-hosted melt inclusions.

These differences suggest that the melt inclusions in olivine and group one clinopyroxene crystallised from a magma distinct from that which produced the inclusions in group three plagioclase and group two clinopyroxene. Höhn et al. (2026) demonstrated that olivine and group one clinopyroxene are not in equilibrium with the majority of the matrix glasses in these samples (i.e. their carrier melt) which have <Mg#40 and are instead in equilibrium with a more primitive magma, identified as the mafic recharge magma. Accordingly, their associated melt inclusions record its chemical composition and evolution via fractional crystallisation. However, it remains unclear whether the most primitive melt inclusions faithfully capture the original composition of the mafic recharge magma or if they have themselves undergone

fractional crystallisation. This uncertainty is underscored by the observation that basaltic enclaves from the 1937 eruption, which have been constrained as the mafic endmember of this volcanic system in magma mixing modelling (Fabbro et al., 2020; Höhn et al., 2026), contain up to 8 wt% MgO, while the most primitive 2014 melt inclusions only contain up to 6 wt% MgO, implying that the latter are likely products of fractional crystallisation.

Höhn et al. (2026) showed that group three plagioclase and group two clinopyroxene are in equilibrium with the majority of the matrix glasses which have <Mg#40 (i.e. the carrier melt) and are therefore interpreted to have crystallised from the evolved, dacitic magma with a composition similar to that of the Rabaul Pyroclastics eruptive products. The melt inclusions hosted in these minerals display chemical compositions that match these more evolved matrix glasses (Fig. 7, Supplementary Fig. S3) and also match the felsic endmember employed in recent magma mixing models (Supplementary Fig. S3) (Höhn et al., 2026). Consequently, these inclusions effectively record the felsic endmember of the magmatic system.

5.2 Volatile saturation pressures

Volatile saturation models use the solubility of volatiles, particularly CO_2, to estimate the pressures at which melt inclusions were entrapped (Blank and Brooker, 1994; Dixon and Stolper, 1995; Shishkina et al., 2010). Nevertheless, these entrapment pressures are only minimum estimates if the melt inclusions either trapped volatile-undersaturated melts or subsequently lost volatiles due to diffusion or decrepitation.

We calculated saturation pressures for clinopyroxene- and olivine-hosted melt inclusions in the 2014 volcanic bombs. First, mineral crystallisation temperatures were calculated using the cpx-

liquid thermometer of Jorgenson et al. (2022) and the olivine-liquid thermometer of Putirka (2008) (eq. 22) with the liquid and mineral compositions being the trapped melt inclusions in the respective host minerals. Calculated temperatures are 1018–1081 °C for clinopyroxene and 1026–1119 °C for olivine. These temperatures were then used as input for the MagmaSat model (Ghiorso and Gualda, 2015) implemented in VESIcal (Iacovino et al., 2021) to calculate the saturation pressures. These calculations yielded saturation pressures of 0.1–1.6 kbar for clinopyroxene and 0.2–1.7 kbar for olivine. Only one olivine produced a higher pressure of 2.8 kbar (Fig. 13). In contrast, while cpx-liquid thermobarometry calculations yielded comparable temperatures between 1000 and 1114°C, they produce higher pressures ranging from 0.8 to 4.4 kbar (Höhn et al., 2026) (Fig. 13). If the melt inclusions were trapped during crystallisation at the higher pressure of >2 kbar, then the difference between the calculated pressures suggests either that the melt inclusions trapped volatile-undersaturated melts, or that they experienced post-entrapment modification of their volatile contents. In either scenario, the calculated volatile saturation pressures should be regarded as minima. Both scenarios are evaluated below.

5.3 Assessing the modification of melt inclusion volatile contents

Decrepitation through Fractures and Recrystallisation

A few of the studied melt inclusions are connected to fractures in the host crystal through which a fluid or vapour phase could have escaped, leading to re-equilibration of the melt inclusions with their external environment during magma ascent (Venugopal et al., 2020b; Rose-Koga et al., 2021). Additionally, the group one and group two plagioclase hosts have cores that seem to have been partially dissolved and then recrystallised, trapping a more evolved, volatile-poor (especially in CO_2) melt. As discussed before, the melt inclusions in these minerals are not primary melt inclusions that were trapped during the original crystallisation of the plagioclase.

Instead, they are secondary melt inclusions trapped during the recrystallisation stage. This means that the volatile contents recorded in these melt inclusions do not represent primary volatile concentrations.

Volatile-Trace Element Systematics

Selected trace elements, like Ce, Nb, Dy and Nd are often used as proxies of volatile abundance because they show similar incompatibility during mantle melting and fractional crystallisation. Hereby, Ce is often used as a proxy for H_2O, Nb for CO_2, Dy for S, and Nd for F (Michael, 1995; Saal et al., 2002; Ruscitto et al., 2012; Muth and Wallace, 2022). These selected trace elements can therefore be used to investigate whether volatiles in melt inclusions were altered during processes such as degassing, diffusion or decrepitation. If a specific volatile species was undersaturated in the melt and behaved as an incompatible element, then we would expect to see near-constant respective volatile-trace-element ratios with increasing K_2O. In contrast, if a specific volatile species was degassing from the melt, we would expect to see a steep decline in the respective volatile-trace element ratios with increasing K_2O.

Olivine-hosted melt inclusions show constant H_2O contents and decreasing H_2O/Ce ratios (Fig. 8a–b). If H_2O was undersaturated in the melt and behaved as an incompatible species during olivine crystallisation, then we would expect to see increasing H_2O contents and near-constant H_2O/Ce with increasing K_2O. If H_2O was degassing, during olivine crystallisation, we would expect to see decreasing H_2O contents and a steep decline in H_2O/Ce with increasing K_2O. The constant H_2O contents and decreasing H_2O/Ce with increasing K_2O suggest that the magma was likely H_2O-saturated during olivine crystallisation. We do not discount the probability that some melt inclusion H_2O contents could have been slightly modified via diffusive exchange with a slightly degassed carrier melt (e.g. Hartley et al., 2015), which could

contribute to the observed scatter in H_2O concentrations.

CO_2 contents are generally low in most melt inclusions. We used the MagmaSat model (Ghiorso and Gualda, 2015) implemented in VESIcal (Iacovino et al., 2021) to calculate closed- and open-system degassing for the olivine-hosted melt inclusion M11_06.10_02.1m which shows the highest CO_2 concentrations of our melt inclusions. Both degassing paths match quite well the CO_2-H_2O contents of the olivine-hosted melt inclusions (Fig. 8g). Minor diffusive H_2O loss (or gain) from some inclusions could have contributed to the observed scatter around the calculated degassing paths. We interpret the CO_2 compositional trends as being consistent with degassing occurring concurrently with crystallisation and melt inclusions trapping. All CO_2/Nb ratios are low, consistent with CO_2 loss prior to inclusions trapping. The sole exception is melt inclusion M11_06.10_02.2, which was used as the starting point for the degassing path (Fig. 8g) and has a CO_2/Nb ratio of 2082. This is the only melt inclusion whose CO_2 content could be interpreted as representing the primary, undegassed mafic endmember melt.

The negative correlation of SO_2 and Dy and the steep decline of S/Dy with increasing K_2O indicates degassing of sulfur during olivine and clinopyroxene crystallisation (Fig. 8c–d). Melt inclusions entrapped in plagioclase and group two clinopyroxene show overall low SO_2 contents. These inclusions record a more degassed melt, with little remaining SO_2 to show a clear trend with Dy.

The continuous positive correlation for Cl and F with K_2O and Nd in mafic melt inclusions implies that Cl and F were not degassing in the 2014 magma and behaved as incompatible elements during crystallisation (Fig. 9). Plagioclase-hosted melt inclusions show scatter in their

F values which could capture apatite crystallisation at a late stage in the magma evolution.

In summary, decreasing melt inclusion CO_2 and SO_2 contents with increasing K_2O indicate continuous CO_2 and SO_2 degassing, both before and during crystallisation and inclusion trapping. Post-entrapment modification of melt inclusion volatile contents likely includes diffusive exchange of H_2O between melt inclusions and their carrier melt, CO_2 exsolution into some bubbles, and decrepitation and vapour loss through fractures. Thus, careful interpretation and modelling are required to reconstruct the original volatile compositions of the primitive Rabaul magma.

5.4 Comparison with melt inclusions from previous eruptions

The H_2O contents of melt inclusions from the 1994 (Roggensack et al., 1996) and 2006 (Bouvet de Maisonneuve et al., 2015) eruption products generally overlap with those from the 2014 samples, except for melt inclusions in clinopyroxene from the 1994 eruption which show higher H_2O concentrations up to 3.5 wt% (Fig. 14). However, it is unclear whether the published melt inclusion data for the 1994 eruption were corrected for post-entrapment crystallisation. Nevertheless, it is unlikely that the PEC corrections would be substantial enough to bring the H_2O values for 1994 pyroxene melt inclusions to the same level as those from the 2014 eruption. The difference in H_2O contents between the 1994 and 2014 melt inclusions could also be a systematic difference stemming from the use of different SIMS instruments.

While all but one of the 1994 and 2006 melt inclusions have CO_2 concentrations below 600 ppm, some olivine- (n=1), plagioclase- (n=4), and clinopyroxene-hosted melt inclusions (n=2)

in the 2014 volcanic bombs have CO_2 concentrations ranging between 622 and 1001 ppm (Fig. 14a). Additionally, melt inclusions from the 2014 volcanic bombs extend towards higher SO_2 values (Fig. 14b). Melt inclusions from previous eruptions generally have SO_2 concentrations below 2500 ppm. The higher SO_2 concentrations in the 2014 melt inclusions up to 6000 ppm are consistent with the more mafic whole rock compositions of these samples compared to the previous eruptions.

No trace element data are available for melt inclusions from the 1994 and 2006 eruptions, making it difficult to assess possible post-entrapment modifications. However, melt inclusions from these two eruptions follow the similar decreasing CO_2 and SO_2 trends as the 2014 melt inclusions indicating that they also captured continuous degassing from the melt (Fig. 14). This means that melt inclusions from previous eruptions likely experienced similar post-entrapment alterations to the melt inclusions in the 2014 eruption products.

5.5 Estimation of the primary volatile contents of the Rabaul magma

We calculated reverse fractional crystallisation models for the most primitive melt inclusions using Petrolog3 (Danyushevsky and Plechov, 2011). The starting composition was the average composition of the four most primitive melt inclusions (Table 2). Calculations were stopped at 10 wt% MgO. Crystallisation was permitted for plagioclase (<8 wt% MgO), olivine, and clinopyroxene. We used the mineral-melt model of Danyushevsky (2001) and performed the calculations at pressures of 2.8–3.4 kbar, which corresponds to 11–13 km, as geophysical observations indicate storage of mafic magma at a depth of ~12 km underneath the Rabaul caldera (Bai and Greenhalgh, 2005). We used the trace element partition coefficients for basaltic liquids of Rollinson and Pease (2021) to model the trace element concentrations in the primary melt. As a result, the primary Rabaul magma is estimated to contain 5.7–5.8 ppm Ce,

0.4 ppm Nb, 1.7 ppm Dy, and 4.6 ppm Nd (Table 2). The concentrations of these trace elements are then used to estimate the primary volatile content in the 2014 Rabaul magma, based on the volatile-trace element ratios outlined in the following sections.

H_2O

In contrast to mid-ocean ridge basalts (MORB), which exhibit a relatively narrow H_2O/Ce range of 150–280 (Michael, 1995), H_2O/Ce ratios in arc magmas are highly variable, because they are influenced by the slab-surface temperature beneath the volcanic arc (Cooper et al., 2012). The H_2O/Ce ratio was determined to be as low as 300 for the Irazú volcano in Costa Rica and as high as 21,000 for Volcano A in Tonga (Cooper et al., 2012).

Cerium is an incompatible element that is not easily modified in arc magmas. We could therefore argue that the melt inclusion with the lowest Ce concentration must represent the most primitive melt. Melt inclusion M11_06.10_02.01 has the lowest Ce content (8 ppm) and 2.6 wt% H_2O, giving a H_2O/Ce ratio of 3323 which is the highest H_2O/Ce ratio of all our analysed melt inclusions. Using this H_2O/Ce ratio and the primitive Ce contents calculated in the reverse fractional crystallisation modelling, we estimate that primitive Rabaul magmas contain 18,941–19,273 ppm (~1.9 wt%) H_2O. On the other hand, we could also argue that the melt inclusion with the highest MgO content has the most primitive composition. Melt inclusion M11_06.02 has the highest MgO content (6.2 wt%) of all analysed melt inclusions; its Ce and H_2O concentrations are 9 ppm and 2.0 wt% respectively. This yields a H_2O/Ce ratio of 2097 and consequently a primary H_2O concentration of 11,953–12,163 ppm (~1.2 wt%).

Despite the variability of H_2O/Ce in arc magmas, Ruscitto et al. (2012) established a statistically significant (within 95% confidence interval) relationship between the H_2O/Ce ratio

and the thermal parameter ϕ, expressed as: $H_2O/Ce = 0.366\ (0.258–0.480) \times \phi + 1898$. This equation, which is based on a geothermometer developed by Plank et al. (2009), gives us another method to estimate the H_2O/Ce ratio for the Rabaul primary magma. From the thermal parameter ϕ=23.1 determined for the New Britain arc (Syracuse and Abers, 2006), we estimate the H_2O/Ce ratio for the Rabaul primary magma to be 1905 ±5. Combining this ratio with the modelled Ce concentrations for the Rabaul primary magma, we derive a H_2O concentration of 10,830 to 11,078 ppm (~1.1 wt%). This is similar to the lower H_2O content that we get from using H_2O/Ce ratios of our analysed melt inclusions. We therefore conclude that the primary Rabaul magma has a H_2O concentration between 1.1 and 1.9 wt%.

CO_2

Due to its low solubility in silicate melts, CO_2 is typically degassed from magmas before melt inclusion entrapment. Thus, melt inclusions are often trapped at crustal pressures after a significant amount of CO_2 has already been lost from the melt (Wallace, 2005; Wallace et al., 2015). The 2014 melt inclusions show clear signs of degassing (Fig. 8). The highest CO_2 concentration measured in the 2014 olivine-hosted melt inclusions is 1001 ppm with an Nb concentration of 0.48 ppm which yields a CO_2/Nb ratio of 2082. Using our estimated Nb concentration of the primary Rabaul magma, we get a CO_2 concentration of 833 ppm. This value is very low in light of estimates that primary arc magmas contain CO_2 concentrations of at least 3000 ppm, likely within the range of 0.6 to 1.3 wt% (Wallace et al., 2015). This would suggest that even the melt inclusions with the highest CO_2 content (1001 ppm) records a degassed composition. Thus, none of our Rabaul 2014 melt inclusions record primary melt CO_2 contents nor preserve primary CO_2/Nb ratios. Thus, we are not able to constrain the CO_2/Nb ratio or the primary CO_2 concentration for Rabaul primary magmas.

Sulfur

Primary sulfur contents in arc magmas are generally higher than in MORB, ranging from 600 to 7000 ppm (Wallace and Edmonds, 2011; Muth and Wallace, 2022). The S/Dy ratio in arc magmas varies significantly, from 90 to 2600, depending on factors such as the sulfur content of the mantle source, the contribution of slab-derived material, and the oxidation state during mantle melting (Muth and Wallace, 2022 and references therein).

In the 2014 eruption, the highest measured sulfur content is 3001 ±888 ppm with a Dy content of 2.5 ppm corresponding to a S/Dy ratio of 845–1556. Using our calculated Dy content of the primary Rabaul magma, we can infer a primary sulfur content of 1437–2645 ppm (0.14–0.26 wt%). Our estimate falls within the global spectrum of observed primary sulfur contents in arc magmas. However, due to the continuous degassing shown by the Rabaul melt inclusions, this is necessarily a minimum estimate for the primary sulfur content of Rabaul primary magmas.

Halogens (Cl and F)

Unlike CO_2 and SO_2, neither chlorine nor fluorine show evidence of degassing in the olivine-hosted melt inclusions from the 2014 eruption, nor evidence of modification by post-entrapment processes. Assuming that Cl and F behaved as perfectly incompatible elements (D=0) in the melt, we used the Rayleigh fractionation equation and the fraction of melt remaining, as determined by the Petrolog3 model, to estimate their concentrations in the primary Rabaul magma. For chlorine, we calculate a primary melt concentration of 392 ±273 ppm, and for fluorine we estimate a concentration of 59 ±11 ppm.

Comparing the volatile content of Rabaul magmas with other arc volcanoes

We compare the H_2O, S and Cl concentrations of the primary Rabaul magma with those of arc magmas worldwide. The comparative data comes from Muth and Wallace (2022), who derived primary compositions for various arc magmas using reverse crystallization modelling in Petrolog3 (for details on the methodology, see supplementary data in Muth et al., 2022). We observe that all H_2O, S, and Cl lie within the global range (Fig. 15). The H_2O and Cl concentrations in Rabaul melt inclusions lie within the lower end of the global arc range. Estimated Rabaul sulfur concentrations span across most of the global primary sulfur range (Fig. 15d). The results indicate that Rabaul's primary magmas are not exceptionally volatile-rich when compared to the global range of primary arc magmas.

5.6 The SO_2 budget of the 2014 Rabaul eruption

The petrological estimates of the SO_2 budget for the 2014 Tavurvur eruption span a wide range. For a plume height of 10 km and an eruption duration of 8 hours, the estimated SO_2 budget is ~21 kt. In contrast, when considering a plume height of 14 km and an eruption duration of 12 hours, the estimated SO_2 budget increases to ~130 kt (Table 1, Fig. 12). However, both the OMI and IASI time series indicate that the main SO_2 plume is concentrated at an altitude of approximately 10 km (Fig. 10b, d, f), implying that the majority of the SO_2 was injected at this height. Moreover, the satellite-derived SO_2 budgets from IASI imagery (19 ±4 kt and 18 ±7 kt) are only marginally higher than that from OMI (17.1 ±2.7 kt), suggesting that the OMI data effectively captured the majority of the SO_2 plume associated with the eruption. Consequently, estimates based on a plume height of 14 km and a duration of 12 hours appear to be significantly overestimated and we conclude that a melt inclusion-derived SO_2 budget of ~21 kt is a more accurate result. The satellite-derived IASI SO_2 budgets are up to 12% higher than those derived from OMI data. When we transfer this uncertainty to the SO_2 budget calculated with the SO_2

concentrations of the plagioclase-hosted melt inclusions, the value is adjusted to 24 kt. This estimate is still within the same order of magnitude as the satellite-derived value of 17.1 kt.

Comparing the high volatile contents in olivine-hosted melt inclusions and the substantially lower SO_2 contents of group three plagioclase-hosted melt inclusions shows that a significant portion of the SO_2 present in the more primitive melt had already been exsolved prior to the eruption. This raises an important question: was the degassed sulfur efficiently vented from the volcanic system, or did it accumulate within the magma plumbing system prior to the eruption? We conclude that the close agreement between the melt inclusion-derived SO_2 estimate and the satellite-derived SO_2 budget suggests that no substantial excess volatile phase was stored in the system before the eruption.

5.7 2014 in the context of the 1994 to present eruption sequence

The 2014 eruption of Tavurvur represents the culmination of a long sequence of unrest and volcanic activity at Rabaul that began with the 1994 twin eruption, the first eruptive event at Rabaul in over 50 years. The 1994 eruption was preceded by a seismic crisis in 1980, during which earthquakes, ground inflation and subsequent modelling of deformation patterns were interpreted as signals of a shallow magma intrusion beneath the Rabaul caldera (Mori and McKee, 1987; Saunders, 2001). A total uplift of approximately 50 mm was recorded at Matupit Island, and a second deformation source was identified in October 1983 on the eastern side of Vulcan (McKee et al., 1984). This crisis likely marked a mafic recharge episode, introducing mafic magma into the shallow, resident magma reservoir. The 1994 eruption was preceded by a period of rapid uplift by a total of ~35 cm over three years, while the 1994 eruption was accompanied by a total subsistence of ~25 cm measured by GPS (Saunders et al., 2023).

Satellite-derived data estimate a SO_2 budget of approximately 350 kt for the 1994 eruption (Rose et al., 1995; Bouvet de Maisonneuve et al., 2015). This is at the lower end of the 10 to 3000 kt SO_2 which have been recorded for eruptions with a VEI of 4 worldwide (Carn et al., 2016). Rose et al. (1995) suggested that the actual SO_2 emissions were higher but that entry of seawater into the vent led to the accumulation of water droplets and ice around ash particles in the eruption plume which limits SO_2 concentrations in the plume.

Following the 1994 event, Rabaul entered a phase of intermittent eruptive activity characterised by periodic explosions and small-to-moderate ash emissions. These episodes, accompanied by minor fluctuations in the deformation signal (<5 cm), have been interpreted as reflecting cycles of volatile build-up before, and stress release after, periodic explosions (Saunders et al., 2023). Notably, the volatile emissions during this period were modest—insufficient to be captured by the global SO_2 monitoring system with satellites at that time having detection limits of ~2–11 kt (Total Ozone Mapping Spectrometer, TOMS) (Carn et al., 2016).

The 2006 eruption was preceded by rapid uplift of a total of ~15 cm over 1.5 years measured by GPS beginning in January 2005, a pattern similar to that observed before the 1994 eruption but on a smaller scale (Saunders et al., 2023). This inflation likely resulted from another, albeit smaller, mafic recharge event, which contributed to the high SO_2 emissions of approximately 230 kt during the 2006 eruption (Bouvet de Maisonneuve et al., 2015). The 2006 eruption was accompanied by a marked subsidence of ~32 cm in ~6 hours with a gravitational rebound of ~5–6 cm taking place over the following 26 days. After this, a period of continuous subsidence began at the caldera with a total subsistence of ~25 cm over 2.5 years (Saunders et al., 2023).

SO_2 emissions were detected nearly continuously from Tavurvur following the 2006 eruption until the end of 2009 (McCormick et al., 2012; Carn et al., 2017). These emissions coincided with a period of variable volcanic activity, marked by periodic explosions, moderate ash emissions, and prolonged caldera subsidence (Global Volcanism Program, 2011; Saunders et al., 2023). The high SO_2 output during this interval of 6–7 kt/day is attributed to degassing from the main magma reservoir, a process facilitated by the 2006 eruption which completely emptied the conduit (Carn et al., 2017; Saunders et al., 2023). The fact that this interval coincides with a period of continuous subsidence adds credence to a notion of high degassing, probably fed by recharging magma, and presumably offsetting any net increase in volume of magma added to the shallow reservoir that would otherwise cause pressurisation and inflation. Volcanic activity subsided in December 2009, and re-inflation at Rabaul commenced shortly thereafter with a total uplift of ~40 cm over 4.5 years until the 2014 eruption (Saunders et al., 2023). Concurrently, SO_2 emissions rapidly declined until mid-2010, when they almost completely ceased. Inspections of the Tavurvur crater revealed a sealed vent which explains why SO_2 emissions had stopped (Saunders et al., 2023).

Our SO_2 budget calculations for the 2014 eruption confirm that this event was not accompanied by high SO_2 emissions. The limited total subsidence of only 6–7 cm (compared to ~25 cm for the 1994 eruption and ~32 cm for the 2006 eruption) recorded after the 2014 eruption (Saunders et al., 2023) have been explained by two factors. First, the shallow, main magma reservoir had already been extensively degassed during the 2006–2009 period, and no subsequent mafic recharge, evidenced by the absence of notable seismic activity, replenished the volatile content. Second, Saunders et al. (2023) suspected that the 2014 eruption involved only the explosion of a relatively small conduit plug, without engaging the main magma reservoir, which would account for its explosive character yet modest SO_2 output. However, our analysis of glassy

bombs erupted in 2014 show quenched, glassy juvenile material rather than the essentially fully crystallised lithic fragments one would expect from the explosion of a cooled conduit plug. The presence of glassy juvenile clasts indicates that at least some molten, albeit probably degassed, magma was involved in the eruption.

In conclusion, although the 2014 Tavurvur eruption was explosive in nature, it was accompanied by relatively low SO_2 emissions compared to the preceding 1994 and 2006 eruptions. This subdued volatile release is primarily the result of extensive prior degassing of the main magma reservoir between late 2006 to late 2009.

6. Conclusions

This study has provided a comprehensive assessment of the volatile evolution and degassing processes of the Rabaul magma system, with a particular focus on the 2014 eruption. Through detailed analysis of melt inclusions hosted in various mineral phases and the application of reverse fractional crystallisation modelling, the research has yielded several important insights into the primary volatile contents and the subsequent modifications experienced during magma ascent and eruption.

Our investigations revealed that melt inclusions hosted in olivine, clinopyroxene and plagioclase captured two distinct magmatic components: melt inclusions in olivine and group one (high Mg#) clinopyroxene sample the mafic recharge magma with relatively high volatile concentrations which follows a fractional crystallisation trend. In contrast, group three plagioclase- and group two (lower Mg#) clinopyroxene-hosted melt inclusions captured the evolved, dacitic magma characterised by lower volatile contents. The compositions of the melt

inclusions suggest that the mafic recharge magma of Rabaul has a composition similar to the basaltic enclaves from the 1937 eruption and that the more evolved, dacitic magma at Rabaul has a composition similar to the Rabaul Pyroclastics eruptive products.

Analyses of volatiles in the melt inclusions indicate that continuous degassing of CO_2 and SO_2 occurred prior to and during the entrapment of melt inclusions. The observed trends in volatile concentrations, particularly the decreasing CO_2 and SO_2 contents with increasing K_2O, confirm that substantial volatile loss occurred during crystallisation. Although the highest measured CO_2 values in the melt inclusions suggest that some remnants of the primary melt may be preserved, the overall record reflects a degassed system, making it difficult to constrain the primary CO_2 concentration. In contrast, the primary H_2O content is more reliably estimated. Multiple approaches, including H_2O/Ce ratio analysis and thermal parameter constraints, converge on a primary H_2O concentration between approximately 1.1 and 1.9 wt%. The sulfur budget, derived from the S/Dy ratios and trace element modelling, suggests that the primary sulfur content in the Rabaul magma falls at the higher end of typical of arc magmas, estimated at 1400–2600 ppm. Positive correlations between Cl and K_2O and F and Nd imply that both halogens were not degassing and behaved as incompatible elements during crystallisation The estimated primary halogen concentrations are around 392 ppm for Cl and near 59 ppm for F. When compared with global data for primary arc magmas, the estimated volatile concentrations suggest that, despite Rabaul's reputation as a prolific gas emitter, the primary Rabaul magma is not exceptionally volatile-rich.

The volatile budgets derived from both the petrological data and satellite observations indicate that the 2014 eruption was accompanied by a substantially lower SO_2 emission (~20 kt) compared to previous events at Rabaul. This subdued gas release is attributed to significant

pre-eruptive degassing of the main magma reservoir between the end of 2006 and the end of 2009.

Aiuppa et al. (2019) ranked Rabaul among the top global emitters (7th for both SO_2 and CO_2 over the time interval 2005–2015). While that ranking correctly reflects the high outgassing observed during the 2005–2010 interval, observations since ~2010, including the very low persistent SO_2 fluxes and the modest SO_2 output during the powerful strombolian 2014 eruption documented here, indicate that Rabaul's contemporary contribution to atmospheric SO_2 (and likely CO_2) has diminished. Thus, although Rabaul retains the historical reputation of being one of the world's highest outgassing volcanoes, that characterisation is not currently representative of its recent behaviour. This contrast highlights the importance of considering time-integrated emissions and monitoring windows when assessing a volcano's global impact. Rankings based on limited time intervals can mask significant temporal variability, so combining continuous satellite monitoring with petrological time-integrated constraints is essential to accurately quantify a volcano's long-term contribution to atmospheric volatile budgets.

CRediT authorship contribution statement

Melina Höhn: Writing – original draft, Writing – review and editing, Project administration, Methodology, Investigation, Formal analysis, Validation, Visualization, Data curation. **Brendan McCormick Kilbride**: Writing – review and editing, Conceptualisation, Project administration, Validation, Supervision. **Margaret Hartley:** Writing – review and editing, Conceptualisation, Methodology, Validation, Supervision. **Mike Burton**: Writing – review and editing, Software. **Ben Esse**: Writing – review and editing, Validation, Formal analysis,

Visualization, Software, Resources. **John B**. **Dikaung**: Resources. **Ima Itikarai**: Resources. **Kila Mulina**: Resources. **Steve Saunders**: Resources. **Mikhail Sindang**: Writing – review and editing, Resources. **Isabelle Taylor**: Writing – review and editing, Validation, Formal analysis, Visualization, Software, Resources. **Edinburgh Ion Microprobe Facility**: Writing – review and editing, Methodology, Investigation.

Funding

This project was supported by a PhD studentship to M. Höhn, funded by the University of Manchester. Access to the NERC Ion Microprobe Facility was supported under award IMF728-0422. M. Hartley acknowledges NERC grant NE/X013642/1. B. Esse acknowledges NERC grants NE/S004106/1 and NE/N018575/1 and the University of Manchester for funding. B. McCormick Kilbride, M. Burton and B. Esse acknowledge funding received from the Centre for Observation and Modelling of Earthquakes, Volcanoes, and Tectonics (COMET), a partnership between UK Universities and the British Geological Survey. I.A. Taylor is funded by the Leverhulme Trust and acknowledges support from COMET.

Data availability

The geochemical data underlying this article are available in the article and its online supplementary material.

The IASI level 1c data are available from EUMETSAT (EUMETSAT, 2009a). The meteorological profiles used within the IASI iterative retrieval are from ECMWF. The IASI level 1c and ECMWF data were accessed at the Centre for Environmental Data Analysis (CEDA) (EUMETSAT, 2009b, 2014, 2021; European Centre for Medium-Range Weather

Forecasts, 2012).

Acknowledgements

We thank Jonathan Fellows and Jasper Berndt-Gerdes for important help with electron microprobe analyses at the University of Manchester, United Kingdom, and the University of Muenster, Germany.

References

Aiuppa, A., Fischer, T.P., Plank, T. and Bani, P., 2019. CO_2 flux emissions from the Earth's most actively degassing volcanoes, 2005-2015. Scientific reports, 9(5442).

Ariskin, A.A. and Barmina, G.S., 1999. An empirical model for the calculation of spinel-melt equilibria in mafic igneous systems at atmospheric pressure: 2. Fe-Ti oxides. Contributions to Mineralogy and Petrology, 134(2-3): 251-263.

Aster, E.M., Wallace, P.J., Moore, L.R., Watkins, J., Gazel, E. and Bodnar, R.J., 2016. Reconstructing CO_2 concentrations in basaltic melt inclusions using Raman analysis of vapor bubbles. Journal of Volcanology and Geothermal Research, 323: 148-162.

Bai, C.-y. and Greenhalgh, S., 2005. 3D multi-step travel time tomography: Imaging the local, deep velocity structure of Rabaul volcano, Papua New Guinea. Physics of the Earth and Planetary Interiors, 151(3-4): 259-275.

Baldwin, S.L., Fitzgerald, P.G. and Webb, L.E., 2012. Tectonics of the New Guinea Region. Annual Review of Earth and Planetary Sciences, 40(1): 495-520.

Bernard, O. and Bouvet de Maisonneuve, C., 2020. Controls on eruption style at Rabaul, Papua New Guinea – Insights from microlites, porosity and permeability measurements. Journal of Volcanology and Geothermal Research, 406(107068).

Blank, J.G. and Brooker, R.A., 1994. Chapter 5. Experimental Studies of Carbon Dioxide in Silicate Melts: Solubility, Speciation, and Stable Carbon Isotope Behaviour. In: M.R. Carroll and J.R. Holloway (Editors), Volatiles in Magmas. Reviews in Mineralogy, pp. 157-186.

Bouvet de Maisonneuve, C., Costa, F., Patia, H. and Huber, C., 2015. Mafic magma replenishment, unrest and eruption in a caldera setting: insights from the 2006 eruption of Rabaul (Papua New Guinea). Geological Society, London, Special Publications,

422(1): 17-39.

Burton, M., Hayer, C., Miller, C. and Christenson, B., 2021. Insights into the 9 December 2019 eruption of Whakaari/White Island from analysis of TROPOMI SO_2 imagery. Science Advances, 7(25).

Carboni, E., Grainger, R., Walker, J., Dudhia, A. and Siddans, R., 2012. A new scheme for sulphur dioxide retrieval from IASI measurements: application to the Eyjafjallajökull eruption of April and May 2010. Atmospheric Chemistry and Physics, 12(23): 11417-11434.

Carn, S.A., Krueger, A.J., Krotkov, N.A., Yang, K. and Evans, K., 2008. Tracking volcanic sulfur dioxide clouds for aviation hazard mitigation. Natural Hazards, 51(2): 325-343.

Carn, S.A., Krueger, A.J., Krotkov, N.A., Yang, K. and Evans, K. 2009. Tracking volcanic sulfur dioxide clouds for aviation hazard mitigation. Natural Hazards, 51(2): 325-343.

Carn, S.A., Clarisse, L. and Prata, A.J., 2016. Multi-decadal satellite measurements of global volcanic degassing. Journal of Volcanology and Geothermal Research, 311: 99-134.

Carn, S.A., Fioletov, V.E., McLinden, C.A., Li, C. and Krotkov, N.A., 2017. A decade of global volcanic SO_2 emissions measured from space. Scientific Reports, 7(44095).

Clarisse, L., Coheur, P.F., Prata, A.J., Hurtmans, D., Razavi, A., Phulpin, T., Hadji-Lazaro, J. and Clerbaux, C., 2008. Tracking and quantifying volcanic SO_2 with IASI, the September 2007 eruption at Jebel at Tair. Atmospheric Chemistry and Physics, 8(24): 7723-7734.

Clarisse, L., Hurtmans, D., Clerbaux, C., Hadji-Lazaro, J., Ngadi, Y. and Coheur, P.F., 2012. Retrieval of sulphur dioxide from the infrared atmospheric sounding interferometer (IASI). Atmospheric Measurement Techniques, 5(3): 581-594.

Clarisse, L., Coheur, P.F., Theys, N., Hurtmans, D. and Clerbaux, C., 2014. The 2011 Nabro eruption, a SO_2 plume height analysis using IASI measurements. Atmospheric Chemistry and Physics, 14(6): 3095-3111.

Clerbaux, C., Boynard, A., Clarisse, L., George, M., Hadji-Lazaro, J., Herbin, H., Hurtmans, D., Pommier, M., Razavi, A., Turquety, S., Wespes, C. and Coheur, P.F., 2009. Monitoring of atmospheric composition using the thermal infrared IASI/MetOp sounder. Atmospheric Chemistry and Physics, 9(16): 6041-6054.

Cohen, M.D., Stunder, B.J.B., Rolph, G.D., Draxler, R.R., Stein, A.F. and Ngan, F., 2015. NOAA's HYSPLIT Atmospheric Transport and Dispersion Modeling System. Bulletin of the American Meteorological Society, 96(12): 2059-2077.

Cooper, L.B., Ruscitto, D.M., Plank, T., Wallace, P.J., Syracuse, E.M. and Manning, C.E., 2012. Global variations in H_2O/Ce: 1. Slab surface temperatures beneath volcanic arcs. Geochemistry, Geophysics, Geosystems, 13(3).

Cunningham, H.S., Turner, S.P., Dosseto, A., Patia, H., Eggins, S.M. and Arculus, R.J., 2009. Temporal Variations in U-series Disequilibria in an Active Caldera, Rabaul, Papua New Guinea. Journal of Petrology, 50(3): 507-529.

Danyushevsky, L.V., 2001. The effect of small amounts of H_2O on crystallisation of mid-ocean ridge and backarc basin magmas. Journal of Volcanology and Geothermal Research, 110(3-4): 265-280.

Danyushevsky, L.V. and Plechov, P., 2011. Petrolog3: Integrated software for modeling crystallization processes. Geochemistry, Geophysics, Geosystems, 12(7).

Dixon, J.B. and Stolper, E.M., 1995. An Experimental Study of Water and Carbon Dioxide Solubilities in Mid-Ocean Ridge Basaltic Liquids. Part II: Applications to Degassing. Journal of Petrology, 36(6): 1633-1646.

Edmonds, M. and Wallace, P.J., 2017. Volatiles and Exsolved Vapor in Volcanic Systems. Elements, 13(1): 29-34.

Edmonds, M. and Woods, A.W., 2018. Exsolved volatiles in magma reservoirs. Journal of Volcanology and Geothermal Research, 368: 13-30.

Esse, B., Burton, M., Hayer, C., Contreras-Arratia, R., Christopher, T., Joseph, E.P., Varnam, M. and Johnson, C., 2023. SO_2 emissions during the 2021 eruption of La Soufrière, St Vincent, revealed with back-trajectory analysis of TROPOMI imagery. Geological Society, London, Special Publications, 539(1): 231-244.

Esse, B., Burton, M., Hayer, C., La Spina, G., Pardo Cofrades, A., Asensio-Ramos, M., Barrancos, J. and Pérez, N., 2025a. Forecasting the evolution of the 2021 Tajogaite eruption, La Palma, with TROPOMI/PlumeTraj-derived SO_2 emission rates. Bulletin of Volcanology, 87(3).

Esse, B., Burton, M., Brenot, H. and Theys, N., 2025b. Insights into eruption dynamics from TROPOMI/PlumeTraj-derived SO_2 emissions during the 2022 eruption of Mauna Loa, Hawai‘i. Bulletin of Volcanology, 87(9).

EUMETSAT: IASI Level 1C – All Spectral Samples – Metop – Global, https://data.eumetsat.int/product/EO:EUM:DAT:METOP:IASIL1C-ALL?query=IASI [data.eumetsat.int] Level 1C - All Spectral Samples - Metop - Global&s=extended# (last access: 18 December 2025), 2009a.

EUMETSAT: IASI atmospheric spectra (L1C product) from the EPS Metop-A satellite: CEDA mirror archive for STFC, NCAS, NCEO. EUMETSAT [data set], https://catalogue.ceda.ac.uk/uuid/ea46600afc4559827f31dbfbb8894c2e [catalogue.ceda.ac.uk] (last access: 18 December 2025), 2009b.

EUMETSAT: IASI atmospheric spectra (L1C product) from the EPS Metop-B satellite: CEDA mirror archive for STFC, NCAS, NCEO. NERC Earth Observation Data Centre [data set], https://catalogue.ceda.ac.uk/uuid/0092c4fe29f76c1b99b4dc19133f361a [catalogue.ceda.ac.uk] (last access: 28 18 December 2025), 2014.

EUMETSAT: IASI atmospheric spectra (L1C product) from the EPS Metop - C satellite: CEDA mirror archive for STFC, NCAS, NCEO. EUMETSAT [data set], https://catalogue.ceda.ac.uk/uuid/58648f7210c84c44a91dc128d8d750d8 [catalogue.ceda.ac.uk] (last access: 18 December 2025), 2021.

European Centre for Medium-Range Weather Forecasts: ECMWF Operational Regular

Gridded Data at 1.125 degrees resolution. NCAS British Atmospheric Data Centre [data set], https://catalogue.ceda.ac.uk/uuid/a67f1b4d9db7b1528b800ed48198bdac [catalogue.ceda.ac.uk] (last access: 18 December 2025), 2012.

Fabbro, G.N., McKee, C.O., Sindang, M.E., Eggins, S.M. and Bouvet de Maisonneuve, C., 2020. Variable mafic recharge across a caldera cycle at Rabaul, Papua New Guinea. Journal of Volcanology and Geothermal Research, 393(106810).

Frezzotti, M.-L., 2001. Silicate-melt inclusions in magmatic rocks: applications to petrology. Lithos, 55(1-4): 273–299.

Ghiorso, M.S. and Gualda, G.A.R., 2015. An H_2O–CO_2 mixed fluid saturation model compatible with rhyolite-MELTS. Contributions to Mineralogy and Petrology, 169(6).

Global Volcanism Program, 1994. Report on Rabaul (Papua New Guinea) (Venzke, E., ed.), Bulletin of the Global Volcanism Network, 19:9: Smithsonian Institution.

Global Volcanism Program, 2006. Report on Rabaul (Papua New Guinea) (Wunderman, R., ed.), Bulletin of the Global Volcanism Network, 31:9: Smithsonian Institution.

Global Volcanism Program, 2007. Report on Rabaul (Papua New Guinea) (Wunderman, R., ed.), Bulletin of the Global Volcanism Network, 32:6: Smithsonian Institution.

Global Volcanism Program, 2011. Report on Rabaul (Papua New Guinea) (Wunderman, R., ed.), Bulletin of the Global Volcanism Network, 36:7: Smithsonian Institution.

Global Volcanism Program, 2013. Report on Rabaul (Papua New Guinea) (Wunderman, R., ed.), Bulletin of the Global Volcanism Network, 38.10: Smithsonian Institution.

Global Volcanism Program, 2014. Report on Rabaul (Papua New Guinea) (GVP Staff, ed.), Bulletin of the Global Volcanism Network, 39:8: Smithsonian Institution.

Global Volcanism Program, 2017. Report on Rabaul (Papua New Guinea) (Crafford, A.E., and Venzke, E., eds.), Bulletin of the Global Volcanism Network, 42:2: Smithsonian Institution.

Global Volcanism Program, 2021. Report on Rabaul (Papua New Guinea) (Sennert, S., ed.), Weekly Volcanic Activity Report, 13 October–19 October 2021: Smithsonian Institution and US Geological Survey.

Global Volcanism Program, 2024. Report on Rabaul (Papua New Guinea) (Senner, S., ed.). Weekly Volcanic Activity Report, 30 October–5 November 2024: Smithsonian Institution and US Geological Survey.

Hartley, M.E., Neave, D.A., Maclennan, J., Edmonds, M. and Thordarson, T., 2015. Diffusive over-hydration of olivine-hosted melt inclusions. Earth and Planetary Science Letters, 425: 168-178.

Hayer, C., Burton, M., Ferrazzini, V., Esse, B. and Di Muro, A., 2023. Unusually high SO_2 emissions and plume height from Piton de la Fournaise volcano during the April 2020 eruption. Bull Volcanol, 85(4): 21.

Heming, R.F., 1974. Geology and Petrology of Rabaul Caldera, Papua New Guinea. Geological Society of America Bulletin, 85(8): 1253–1264.

Hohl, S.V., Schuth, S., Münker, C., König, S., Garbe-Schönberg, D. and Kuduon, J., 2022. Geochemical evolution of the Rabaul volcanic complex, Papua New Guinea – Insights from HFSE, Sr-Nd-Hf, and Fe isotopes. Lithos, 408-409.

Höhn, M., Hartley, M.E., Dikaung, J.B., Itikarai, I., Mulina, K., Saunders, S., Sindang, M. and McCormick Kilbride, B.T., 2026. Petrological insights into magma storage and evolution at Rabaul Caldera, Papua New Guinea. EarthArXiv Preprint. https://www.doi.org/10.31223/X55T9N.

Holm, R.J., Rosenbaum, G. and Richards, S.W., 2016. Post 8 Ma reconstruction of Papua New Guinea and Solomon Islands: Microplate tectonics in a convergent plate boundary setting. Earth-Science Reviews, 156: 66–81.

Huppert, H.E. and Woods, A.W., 2020. The role of volatiles in magma chamber dynamics. Nature, 420(6915).

Iacovino, K., Matthews, S., Wieser, P.E., Moore, G.M. and Bégué, F., 2021. VESIcal Part I: An Open-Source Thermodynamic Model Engine for Mixed Volatile (H_2O-CO_2) Solubility in Silicate Melts. Earth and Space Science, 8(11).

Johnson, R.W., 2013. Eruptions at Rabaul: 1994–1999, Fire Mountains of the Islands: A History of Volcanic Eruptions and Disaster Management in Papua New Guinea and the Solomon Islands. ANU Press.

Jorgenson, C., Higgins, O., Petrelli, M., Begue, F. and Caricchi, L., 2022. A Machine Learning-Based Approach to Clinopyroxene Thermobarometry: Model Optimization and Distribution for Use in Earth Sciences. Journal of Geological Research: Solid Earth, 127(4).

Kent, A.J.R., 2008. Melt Inclusions in Basaltic and Related Volcanic Rocks. Reviews in Mineralogy and Geochemistry, 69(1): 273-331.

La Spina, G., Arzilli, F., Burton, M.R., Polacci, M. and Clarke, A.B., 2022. Role of volatiles in highly explosive basaltic eruptions. Communications Earth & Environment, 3(1).

Langmuir, C.H., Klein, E.M. and Plank, T., 1992. Petrological Systematics of Mid-Ocean Ridge Basalts: Constraints on Melt Generation Beneath Ocean Ridges, Mantle Flow and Melt Generation at Mid-Ocean Ridges. Geophysical Monograph Series, pp. 183-280.

Levelt, P.F., van den Oord, G.H.J., Dobber, M.R., Malkki, A., Huib, V., Johan de, V., Stammes, P., Lundell, J.O.V. and Saari, H., 2006. The ozone monitoring instrument. IEEE Transactions on Geoscience and Remote Sensing, 44(5): 1093-1101.

Li, C., Krotkov, N.A., Leonard, P.J.T., Carn, S., Joiner, J., Spurr, R.J.D. and Vasilikov, A., 2020. Version 2 Ozone Monitoring Instrument SO_2 product (OMSO2 V2): new anthropogenic SO_2 vertical column density dataset. Atmospheric Measurement Techniques, 11(13): 6175-6191.

Lowenstern, J.B., 2003. Melt inclusions come of age: Volatiles, volcanoes, and sorby's legacy, Melt Inclusions in Volcanic Systems – Methods, Applications and Problems. Developments in Volcanology, pp. 1-21.

Maclennan, J., 2017. Bubble formation and decrepitation control the CO_2 content of olivine-hosted melt inclusions. Geochemistry, Geophysics, Geosystems, 18(2): 597-616.

Mastin, L.G., Guffanti, M., Servranckx, R., Webley, P., Barsotti, S., Dean, K., Durant, A., Ewert, J.W., Neri, A., Rose, W.I., Schneider, D., Siebert, L., Stunder, B., Swanson, G., Tupper, A., Volentik, A. and Waythomas, C.F., 2009. A multidisciplinary effort to assign realistic source parameters to models of volcanic ash-cloud transport and dispersion during eruptions. Journal of Volcanology and Geothermal Research, 186(1-2): 10-21.

McCormick, B.T., Edmonds, M., Mather, T.A. and Carn, S.A., 2012. First synoptic analysis of volcanic degassing in Papua New Guinea. Geochemistry, Geophysics, Geosystems, 13(3).

McCormick, B.T., Herzog, M., Yang, J., Edmonds, M., Mather, T.A., Carn, S.A., Hidalgo, S. and Langmann, B., 2014. A comparison of satellite- and ground-based measurements of SO_2 emissions from Tungurahua volcano, Ecuador. Journal of Geophysical Research: Atmospheres, 119(7): 4264-4285.

McCormick, B., Popp, C., Andrews, B. and Cottrell, E., 2015. Ten years of satellite observations reveal highly variable sulphur dioxide emissions at Anatahan Volcano, Mariana Islands. Journal of Geophysical Research: Atmospheres, 120(14): 7258-7282.

McCormick Kilbride, B.T., Barry, P.H., Fischer, T.P., Holland, G., Hudak, M., Nowicki, S., Ballentine, C., Fox, M.D., Höhn, M., Itikarai, I., Johnson, M.D., Mulina, K. and Nicholson, E.J., 2024. Helium, carbon and nitrogen isotope evidence for slab influence on volcanic gas emissions at Rabaul caldera, Papua New Guinea. Chemical Geology, 670.

McKee, C.O., Lowenstein, P.L., Saint Ours, P., Talai, B., Itikarai, I. and Mori, J.J., 1984. Seismic and ground deformation crises at Rabaul Caldera: Prelude to an eruption? Bulletin Volcanologique, 47(2): 397-411.

McKee, C.O., Baillie, M.G. and Reimer, P.J., 2015. A revised age of ad 667–699 for the latest major eruption at Rabaul. Bulletin of Volcanology, 77(7).

McKee, C.O. and Duncan, R.A., 2016. Early volcanic history of the Rabaul area. Bulletin of Volcanology, 78(24).

Metrich, N. and Wallace, P.J., 2008. Volatile Abundances in Basaltic Magmas and Their Degassing Paths Tracked by Melt Inclusions. Reviews in Mineralogy and Geochemistry, 69(1): 363-402.

Michael, P., 1995. Regionally distinctive sources of depleted MORB: Evidence from trace elements and H_2O. Earth and Planetary Science Letters, 131(3-4): 301-320.

Moore, L.R., Gazel, E., Tuohy, R., Lloyd, A.S., Esposito, R., Steele-MacInnis, M., Hauri, E.H., Wallace, P.J., Plank, T. and Bodnar, R.J., 2015. Bubbles matter: An assessment of the

contribution of vapor bubbles to melt inclusion volatile budgets. American Mineralogist, 100(4): 806-823.

Mori, J. and McKee, C., 1987. Outward-dipping ring-fault structure at rabaul caldera as shown by earthquake locations. Science, 235(4785): 193-195.

Muth, M.J. and Wallace, P.J., 2022. Sulfur recycling in subduction zones and the oxygen fugacity of mafic arc magmas. Earth and Planetary Science Letters, 599.

Nairn, I.A., Wood, C.P., Talai, B. and Mckee, C.O., 1989. Rabaul Caldera, Papua New Guinea—125,000 reconnaissance Geological Map and Eruption History, New Zealand Geological Survey.

Nairn, I.A., McKee, C.O., Talai, B. and Wood, C.P., 1995. Geology and eruptive history of the Rabaul Caldera area, Papua New Guinea. Journal of Volcanology and Geothermal Research, 69(3-4): 255–284.

Pardini, F., Burton, M., Arzilli, F., La Spina, G. and Polacci, M., 2018. SO_2 emissions, plume heights and magmatic processes inferred from satellite data: The 2015 Calbuco eruptions. Journal of Volcanology and Geothermal Research, 361: 12-24.

Patia, H., 2004. Petrology and geochemistry of the recent eruption history at Rabaul Caldera, Papua New Guinea: implications for magmatic processes and recurring volcanic activity. M.Sc Thesis, University of Papua New Guinea, Port Moresby.

Patia, H., Eggins, S.M., Arculus, R.J., McKee, C.O., Johnson, R.W. and Bradney, A., 2017. The 1994–2001 eruptive period at Rabaul, Papua New Guinea: Petrological and geochemical evidence for basalt injections into a shallow dacite magma reservoir, and significant SO_2 flux. Journal of Volcanology and Geothermal Research, 345: 200–217.

Petrelli, M., Caricchi, L. and Perugini, D., 2020. Machine Learning Thermo-Barometry: Application to Clinopyroxene-Bearing Magmas. Journal of Geophysical Research: Solid Earth, 125.

Plank, T., Cooper, L.B. and Manning, C.E., 2009. Emerging geothermometers for estimating slab surface temperatures. Nature Geoscience, 2(9): 611-615.

Putirka, K.D., 2008. Thermometers and Barometers for Volcanic Systems. Reviews in Mineralogy and Geochemistry, 69: 61-120.

Queisser, M., Burton, M., Theys, N., Pardini, F., Salerno, G., Caltabiano, T., Varnam, M., Esse, B. and Kazahaya, R., 2019. TROPOMI enables high resolution SO_2 flux observations from Mt. Etna, Italy, and beyond. Scientific Reports, 9(1): 957.

Roedder, E., 1984. Occurrence and significance of magmatic inclusions and silicate liquid immiscibility. Acta Geologica Polonica, 34: 139–178.

Roggensack, Williams, Schaefer and Parnell, 1996. Volatiles from the 1994 Eruptions of Rabaul: Understanding Large Caldera Systems. Science, 273(5274): 490–493.

Rollinson, H. and Pease, V., 2021. Using Geochemical Data. Cambridge University Press.

Rose, W.I., Delene, D.J., Schneider, D.J., Bluth, G.J.S., Krueger, A.J., Sprod, I., McKee, C., Davies, H.L. and Ernst, G.G.J., 1995. Ice in the 1994 Rabaul eruption cloud: implications for volcano hazard and atmospheric effects. Nature, 375(6531): 477-479.

Rose-Koga, E.F., Bouvier, A.S., Gaetani, G.A., Wallace, P.J., Allison, C.M., Andrys, J.A., Angeles de la Torre, C.A., Barth, A., Bodnar, R.J., Bracco Gartner, A.J.J., Butters, D., Castillejo, A., Chilson-Parks, B., Choudhary, B.R., Cluzel, N., Cole, M., Cottrell, E., Daly, A., Danyushevsky, L.V., DeVitre, C.L., Drignon, M.J., France, L., Gaborieau, M., Garcia, M.O., Gatti, E., Genske, F.S., Hartley, M.E., Hughes, E.C., Iveson, A.A., Johnson, E.R., Jones, M., Kagoshima, T., Katzir, Y., Kawaguchi, M., Kawamoto, T., Kelley, K.A., Koornneef, J.M., Kurz, M.D., Laubier, M., Layne, G.D., Lerner, A., Lin, K.Y., Liu, P.P., Lorenzo-Merino, A., Luciani, N., Magalhães, N., Marschall, H.R., Michael, P.J., Monteleone, B.D., Moore, L.R., Moussallam, Y., Muth, M., Myers, M.L., Narváez, D.F., Navon, O., Newcombe, M.E., Nichols, A.R.L., Nielsen, R.L., Pamukcu, A., Plank, T., Rasmussen, D.J., Roberge, J., Schiavi, F., Schwartz, D., Shimizu, K., Shimizu, K., Shimizu, N., Thomas, J.B., Thompson, G.T., Tucker, J.M., Ustunisik, G., Waelkens, C., Zhang, Y. and Zhou, T., 2021. Silicate melt inclusions in the new millennium: A review of recommended practices for preparation, analysis, and data presentation. Chemical Geology, 570.

Ruscitto, D.M., Wallace, P.J., Cooper, L.B. and Plank, T., 2012. Global variations in H_2O/Ce: 2. Relationships to arc magma geochemistry and volatile fluxes. Geochemistry, Geophysics, Geosystems, 13(3).

Ruth, D.C.S., Costa, F., Bouvet de Maisonneuve, C., Franco, L., Cortes, J.A. and Calder, E.S., 2018. Crystal and melt inclusion timescales reveal the evolution of magma migration before eruption. Nature Communications, 9(1): 2657.

Saal, A.E., Hauri, E.H., Langmuir, C.H. and Perfit, M.R., 2002. Vapour undersaturation in primitive mid-ocean-ridge basalt and the volatile content of Earth's upper mantle. Nature, 419(6906): 451-455.

Saunders, S.J., 2001. The shallow plumbing system of Rabaul caldera: a partially intruded ring fault? Bulletin of Volcanology, 63(6): 406-420.

Saunders, S., Tenor, E., Wakawa, J. and Nohou, J., 2023. Twenty-Two Years of GPS Monitoring at Rabaul Caldera, a Narrative History. Geosciences, 13(8).

Schiano, P., 2003. Primitive mantle magmas recorded as silicate melt inclusions in igneous minerals. Earth-Science Reviews, 63(1-2): 121-144.

Scholz, K., Townsend, M., Huber, C., Troch, J., Bachmann, O. and Coonin, A.N., 2023. Investigating the Impact of an Exsolved H_2O-CO_2 Phase on Magma Chamber Growth and Longevity: A Thermomechanical Model. Geochemistry, Geophysics, Geosystems, 24(12).

Shishkina, T.A., Botcharnikov, R.E., Holtz, F., Almeev, R.R. and Portnyagin, M.V., 2010. Solubility of H_2O- and CO_2-bearing fluids in tholeiitic basalts at pressures up to 500MPa. Chemical Geology, 277(1-2): 115-125.

Steele-MacInnis, M., Esposito, R., Moore, L.R. and Hartley, M.E., 2017. Heterogeneously

entrapped, vapor-rich melt inclusions record pre-eruptive magmatic volatile contents. Contributions to Mineralogy and Petrology, 172(4).

Syracuse, E.M. and Abers, G.A., 2006. Global compilation of variations in slab depth beneath arc volcanoes and implications. Geochemistry, Geophysics, Geosystems, 7(5).

Tait, S., Jaupart, C. and Vergniolle, S., 1989. Pressure, gas content and eruption periodicity of a shallow, crystallising magma chamber. Earth and Planetary Science Letters, 92(1): 107-123.

Torres, O., Bhartia, P.K., Jethva, H. and Ahn, C., 2018. Impact of the ozone monitoring instrument row anomaly on the long-term record of aerosol products. Atmospheric Measurement Techniques, 11(5): 2701-2715.

Tupper, A. and Wunderman, R., 2009. Reducing discrepancies in ground and satellite-observed eruption heights. Journal of Volcanology and Geothermal Research, 186(1-2): 22-31.

Venugopal, S., Moune, S., Williams-Jones, G., Druitt, T., Vigouroux, N., Wilson, A. and Russell, J.K., 2020a. Two distinct mantle sources beneath the Garibaldi Volcanic Belt: Insight from olivine-hosted melt inclusions. Chemical Geology, 532.

Venugopal, S., Schiavi, F., Moune, S., Bolfan-Casanova, N., Druitt, T.H. and Williams-Jones, G., 2020b. Melt inclusion vapour bubbles: the hidden reservoir for major and volatile elements. Scientific Reports, 10(1): 9034.

Walker, J.C., Dudhia, A. and Carboni, E., 2011. An effective method for the detection of trace species demonstrated using the MetOp Infrared Atmospheric Sounding Interferometer. Atmospheric Measurement Techniques, 4(8): 1567-1580.

Walker, J.C., Carboni, E., Dudhia, A. and Grainger, R.G., 2012. Improved detection of sulphur dioxide in volcanic plumes using satellite-based hyperspectral infrared measurements: Application to the Eyjafjallajökull 2010 eruption. Journal of Geophysical Research: Atmospheres, 117(D20).

Wallace, P.J., 2005. Volatiles in subduction zone magmas: concentrations and fluxes based on melt inclusion and volcanic gas data. Journal of Volcanology and Geothermal Research, 140(1-3): 217-240.

Wallace, P.J. and Edmonds, M., 2011. The Sulfur Budget in Magmas: Evidence from Melt Inclusions, Submarine Glasses, and Volcanic Gas Emissions. Reviews in Mineralogy and Geochemistry, 73(1): 215-246.

Wallace, P.J., Plank, T., Edmonds, M. and Hauri, E.H., 2015. Volatiles in Magmas. In: H. Sigurdsson (Editor), The Encyclopedia of Volcanoes. Academic Press, pp. 163-183.

Wieser, P., Petrelli, M., Lubbers, J., Wieser, E., Ozaydin, S., Kent, A. and Till, C., 2022. Thermobar: An open-source Python3 tool for thermobarometry and hygrometry. Volcanica, 5(2): 349-384.

Wood, C.P., Nairn, I.A., Mckee, C.O. and Talai, B., 1995. Petrology of the Rabaul Caldera area, Papua New Guinea. Journal of Volcanology and Geothermal Research, 69(3-4): 285–302.

Zhang, L., Ren, Z.Y., Xia, X.P., Yang, Q., Hong, L.B. and Wu, D., 2019. In situ determination of trace elements in melt inclusions using laser ablation inductively coupled plasma sector field mass spectrometry. Rapid Communications in Mass Spectrometry, 33(4): 361-370.

Table 1: OMI and IASI derived parameters for calculation of mass of erupted SO_2 during the 2014 eruption of Tavurvur.

Calculation parameters	OMI derived parameters	IASI derived parameters
Plume height	10 km	14 km
Mass Eruption Rate (MER)	2.0×10^6 kgs^{-1}	8.0×10^6 kgs^{-1}
Eruption Duration	8 hours	12 hours
Mass of erupted magma	5.7×10^{10} kg	3.5×10^{11} kg
Crystallinity of melt	0.38	0.38
Mass of erupted melt	3.5×10^{10} kg	2.1×10^{11} kg
Mass of erupted SO_2 calculated with petrological method	21 kt	130 kt

Table 2: Start and end compositions for reverse fractional crystallisation modelling.

	Start Composition	**End Composition**		
modelling pressure (kbar)		2.8	3.0	3.4
SiO_2	48.05	48.28	48.27	48.24
TiO_2	1.39	0.81	0.82	0.83
Al_2O_3	16.73	15.46	15.50	15.58
Fe_2O_3		0.73	0.74	0.76
FeO	9.53*	6.43	6.47	6.55
MnO	0.20	0.16	0.16	0.16
MgO	6.03	10.00	10.00	10.00
CaO	12.80	14.70	14.61	14.41
Na_2O	2.14	1.49	1.51	1.54
K_2O	0.57	0.31	0.31	0.32
P_2O_5	0.12	0.07	0.07	0.07
Cr_2O_3	0.01	0.26	0.25	0.24
H_2O	2.29	1.25	1.26	1.28
Total	99.88	99.95	99.95	99.95
Sr	467.63	263.7	265.5	269.5
Y	16.22	11.7	11.7	11.7
Zr	34.42	19.5	19.6	19.9
Nb	0.66	0.4	0.4	0.4
Ba	117.22	67.7	68.2	69.3
La	3.97	2.3	2.3	2.3
Ce	9.75	5.7	5.7	5.8
Nd	7.56	4.6	4.6	4.6
Sm	1.89	1.2	1.2	1.2
Eu	0.21	0.1	0.1	0.1
Gd	2.35	1.6	1.6	1.6
Dy	2.51	1.7	1.7	1.7
Yb	1.24	0.8	0.8	0.8
Th	0.26	0.1	0.1	0.1

* FeO_T

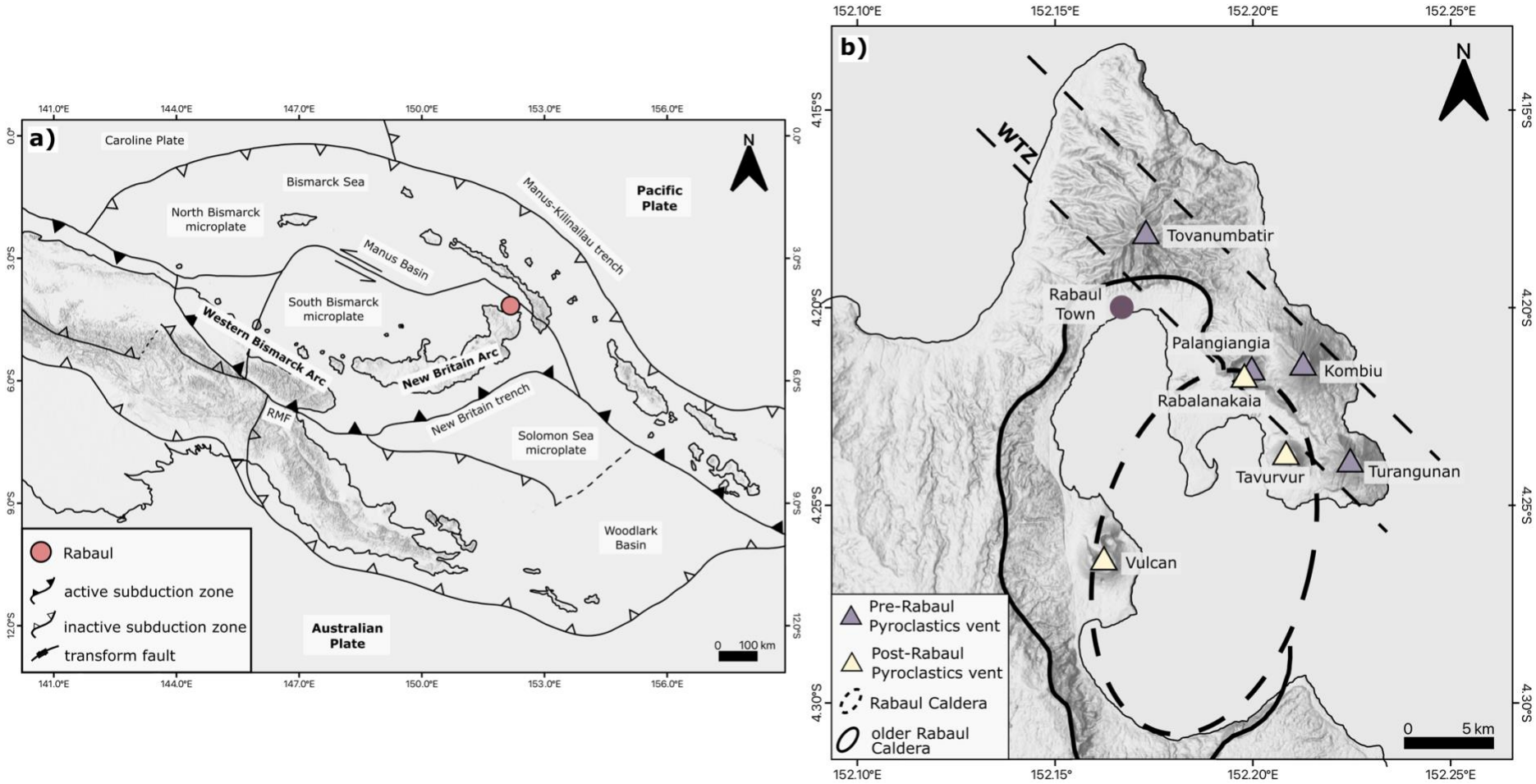

Figure 1: a) Tectonic setting of New Britain Island (after Höhn et al., 2026). RMF = Ramu-Marham fault. **b)** Overview of the Rabaul Caldera Complex (after Höhn et al., 2026). WTZ = Watom-Turangunan-Zone

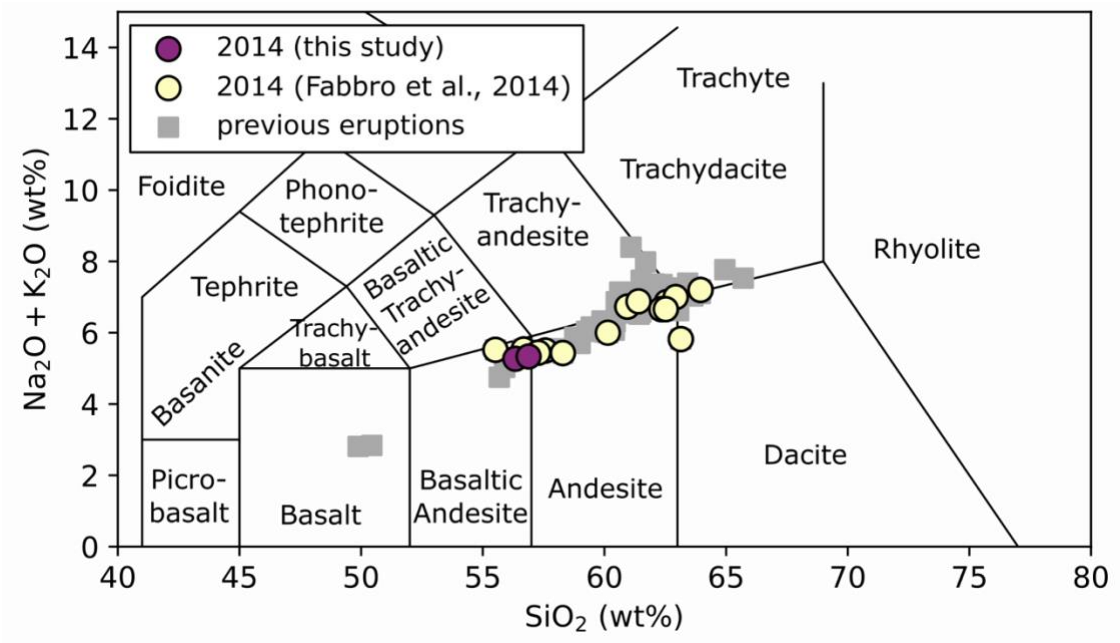

Figure 2: TAS diagram comparing whole rock compositions of the samples from this study (Höhn et al., 2026) with literature data for the 2014 eruption (Fabbro et al., 2020) and whole rock compositions from other Post-Rabaul Pyroclastics eruptions at Rabaul (Nairn et al., 1989; Cunningham et al., 2009; Bouvet de Maisonneuve et al., 2015; Patia et al., 2017; Bernard and Bouvet de Maisonneuve, 2020; Fabbro et al., 2020; Hohl et al., 2022).

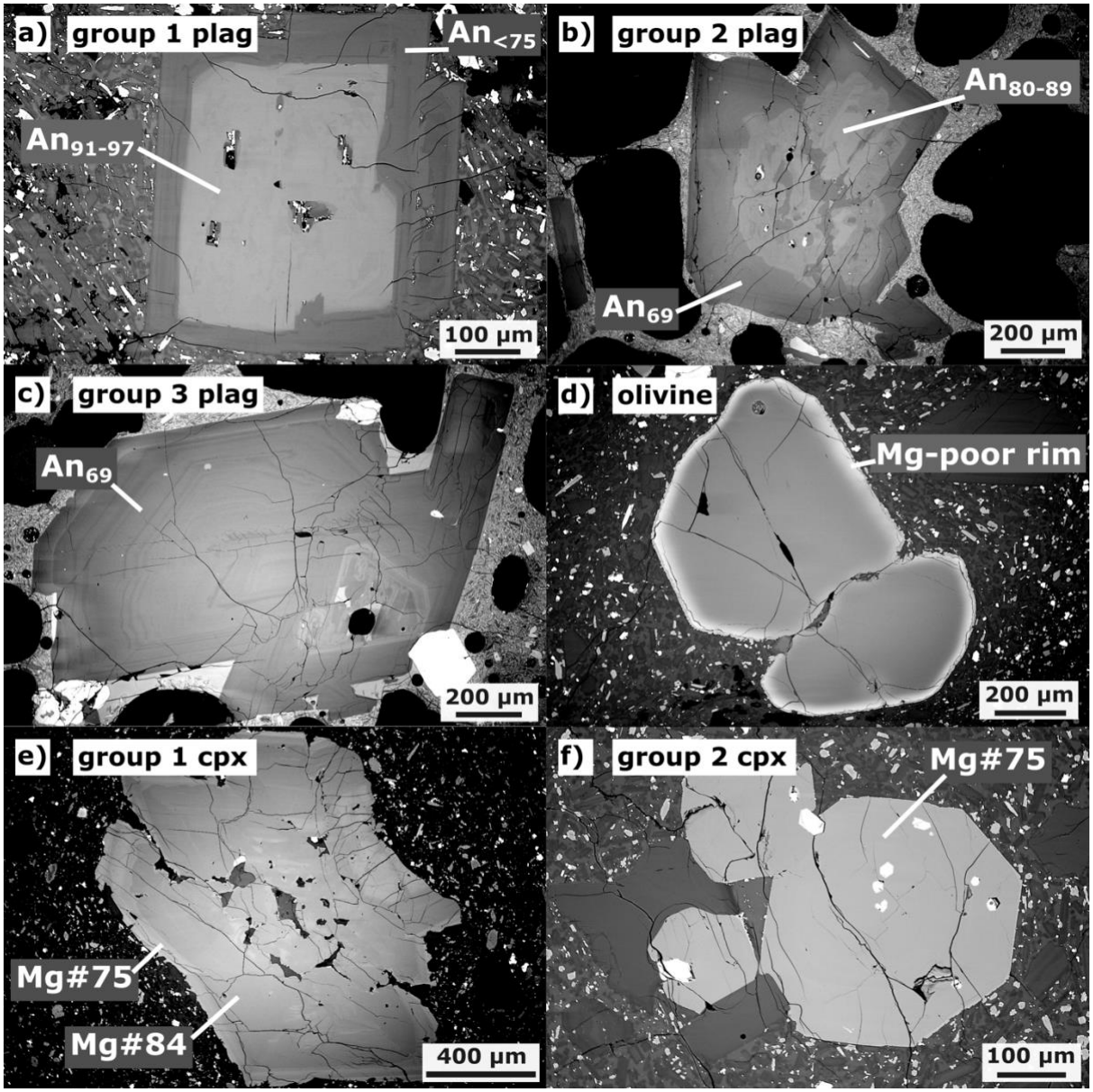

Figure 3: BSE images of **a)** group one plagioclase, **b)** group two plagioclase, **c)** group three plagioclase, **d)** olivine, **e)** group one clinopyroxene, and **f)** group two clinopyroxene in the Rabaul eruption products (after Höhn et al., 2026).

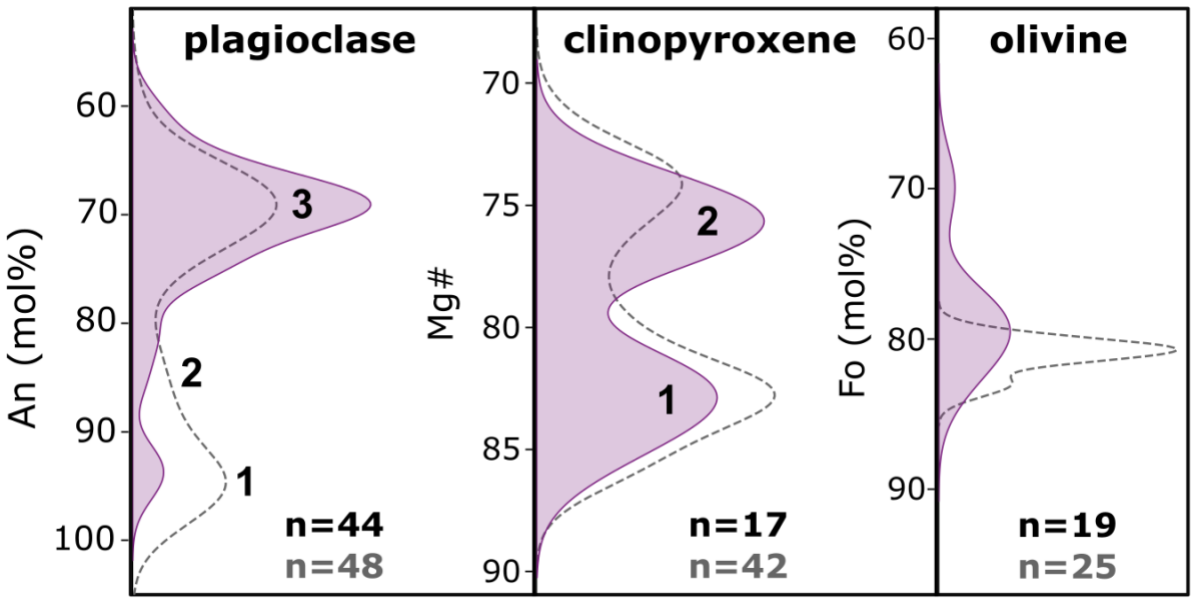

Figure 4: Anorthite (An), Mg#, and forsterite (Fo) contents in plagioclase, clinopyroxene and olivine cores from melt inclusion host minerals (purple shaded curves) compared to mineral chemistry data for the 2014 volcanic bombs from Höhn et al. (2026) (dashed lines). The numbers mark the peaks of the different groups of plagioclase and clinopyroxene. Number of analyses are given in black (melt inclusion host minerals, this study) and grey (mineral data, Höhn et al., 2026).

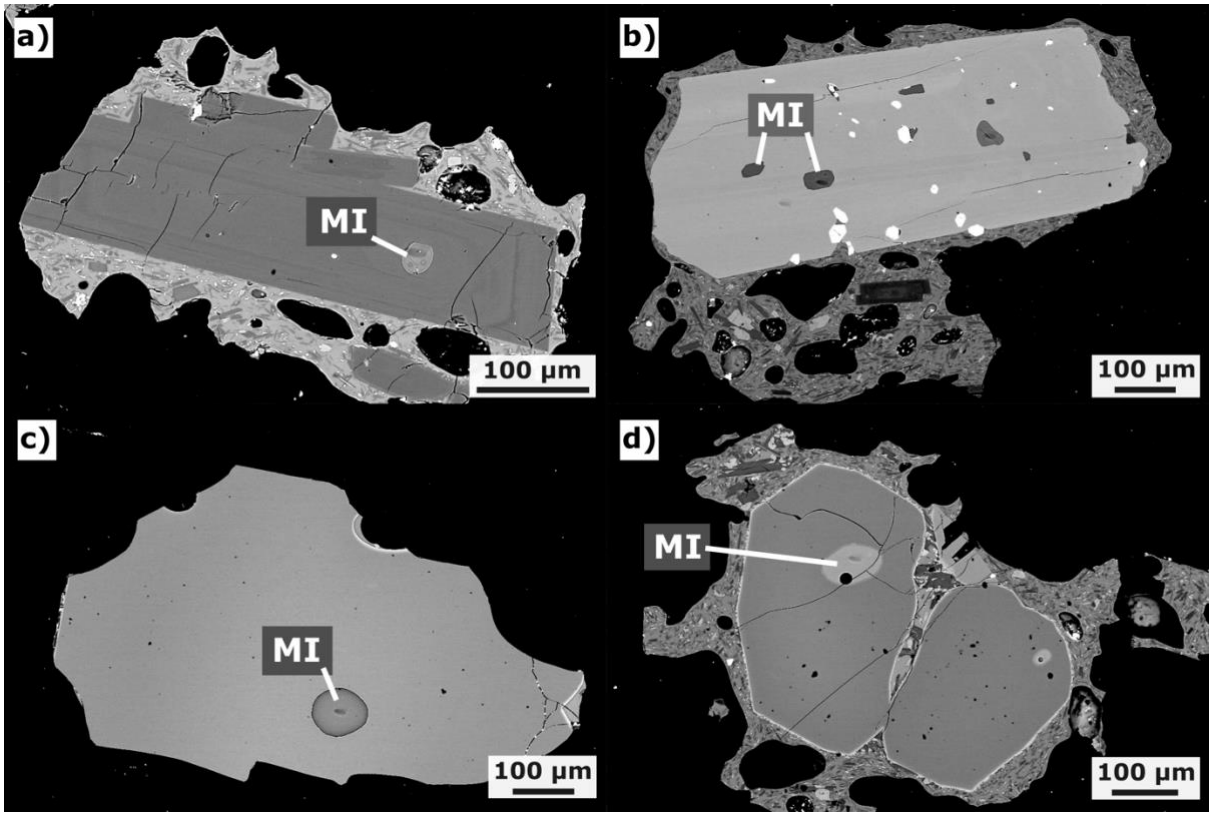

Figure 5: BSE images of melt inclusions (MI) in **a)** plagioclase, **b)** clinopyroxene, and **c–d)** olivine in the 2014 volcanic bombs.

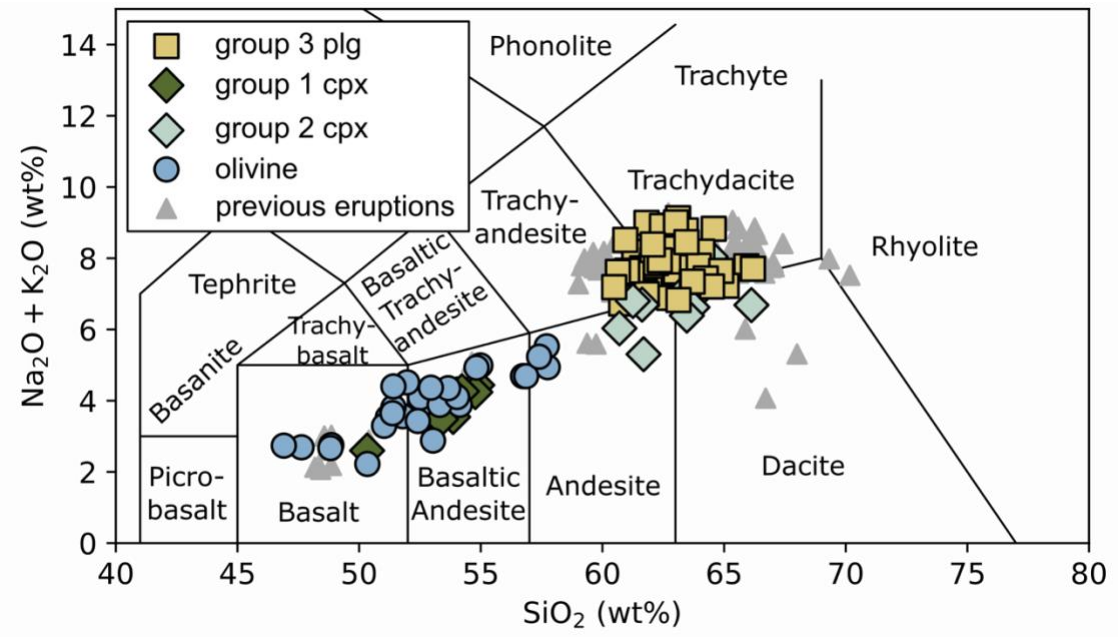

Figure 6: TAS diagram comparing plagioclase-, clinopyroxene-, and olivine-hosted melt inclusions in the 2014 eruption products with those of previous eruptions. The data for previous eruptions include olivine- and pyroxene-hosted melt inclusions from the 1994 eruption (Roggensack et al., 1996) and plagioclase- and pyroxene-hosted melt inclusions from the 2006 eruption (Bouvet de Maisonneuve et al., 2015). Shown here are PEC corrected values for the 2006 and 2014 eruptions. plg = plagioclase, cpx = clinopyroxene.

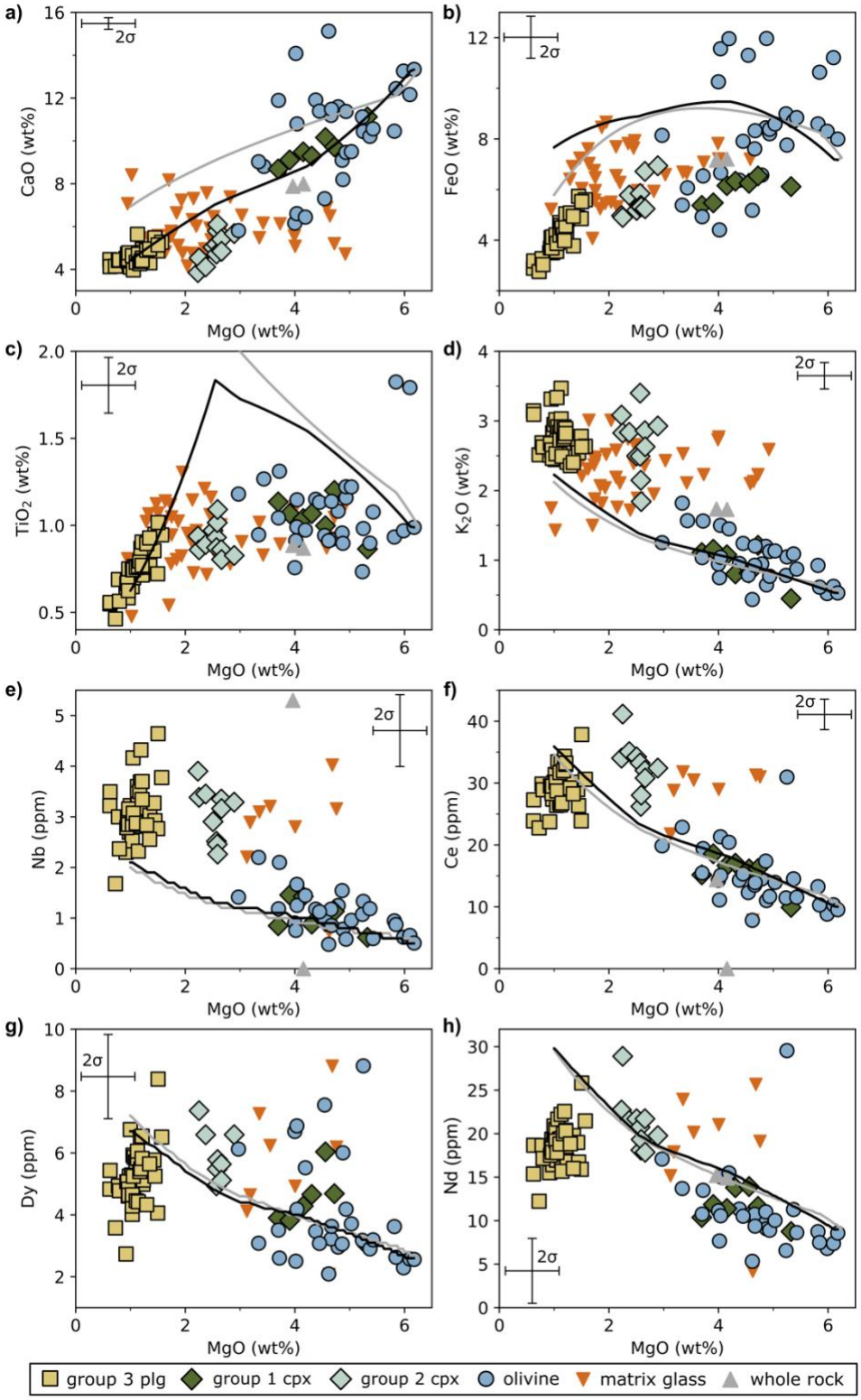

Figure 7: Selected major and trace elements for plagioclase- (yellow squares), clinopyroxene- (green diamonds), and olivine-hosted (blue circles) melt inclusions and matrix glass (orange downward arrows) in the 2014 volcanic bombs. Shown here are PEC corrected values. Whole rock compositions for the 2014 volcanic bombs are shown in grey triangles. Errors bars indicate 2σ uncertainties. Grey and black lines are results of fractional crystallisation modelling with Petrolog3 (Danyushevsky and Plechov, 2011) with the mineral-melt equilibrium models of Langmuir et al. (1992) (grey line) and Danyushevsky (2001) (black line). Whole rock compositions and major element data for matrix glasses are from Höhn et al. (2026).

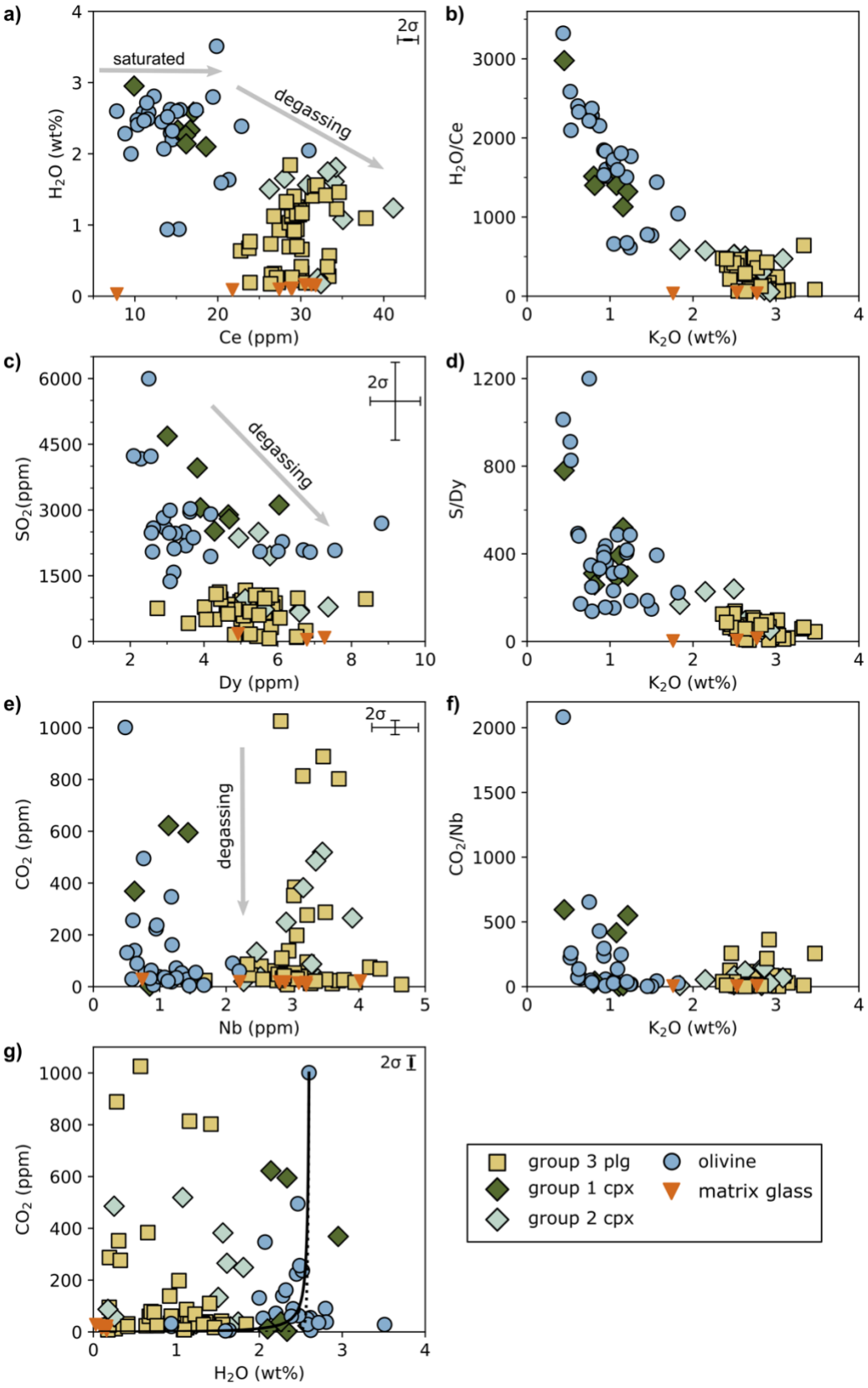

Figure 8: a–b) H_2O, **c–d)** SO_2, and **e–h)** CO_2 variation diagrams for plagioclase-, clinopyroxene-, and olivine-hosted melt inclusions and matrix glass in the 2014 volcanic bombs. Solid- and dotted lines in g) represent closed- and open-system degassing paths starting at basaltic olivine-hosted melt inclusion M11_06.10.02.1 calculated with VESIcal (Iacovino et al., 2021) with the MagmaSat model (Ghiorso and Gualda, 2015). Shown here are PEC corrected values. Error bars indicate 2σ uncertainties.

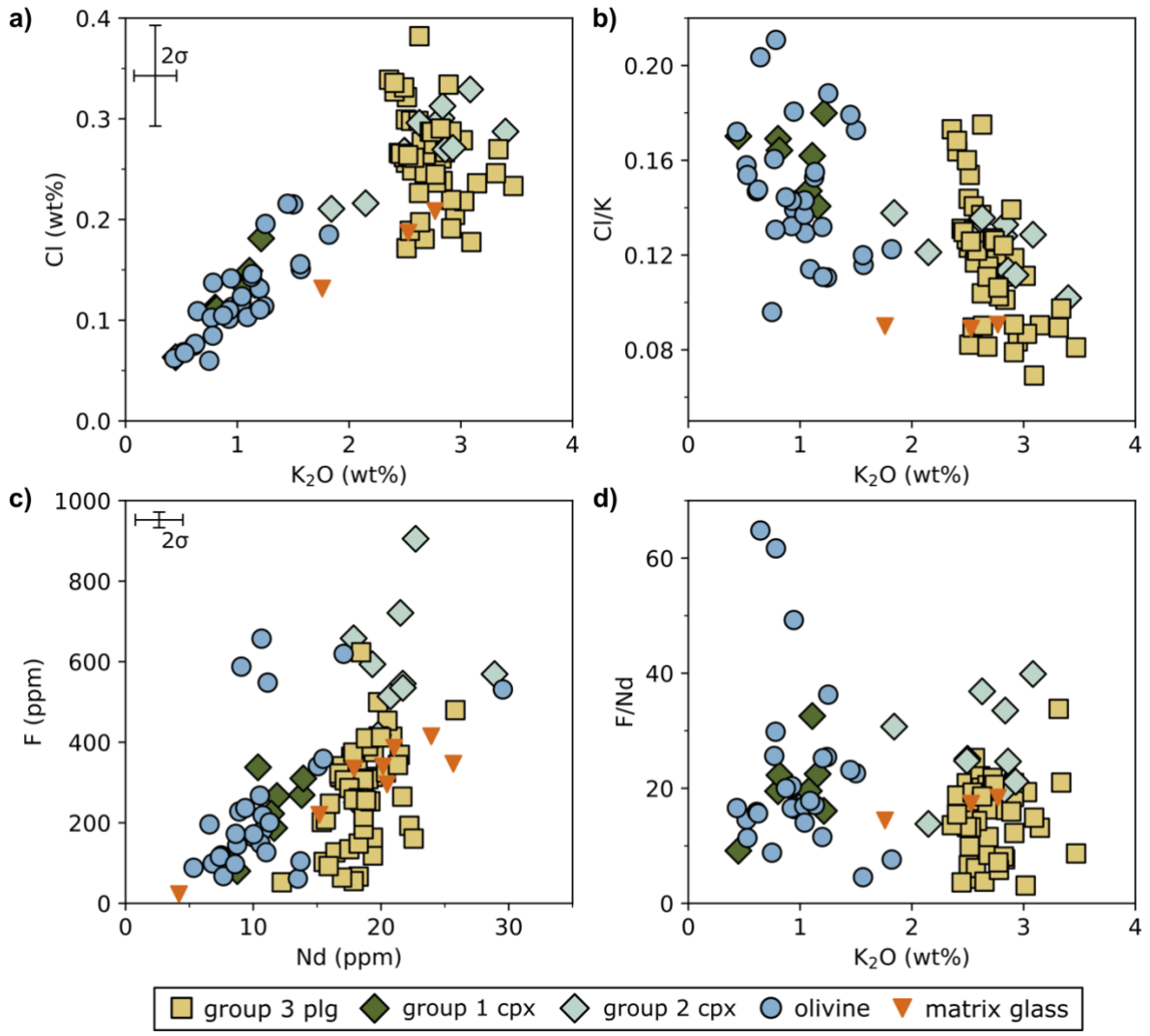

Figure 9: a–b) Cl, and **c–d)** F variation diagrams for plagioclase-, clinopyroxene-, and olivine-hosted melt inclusions and matrix glass in the 2014 volcanic bombs. Shown here are PEC corrected values. Error bars indicate 2σ uncertainties.

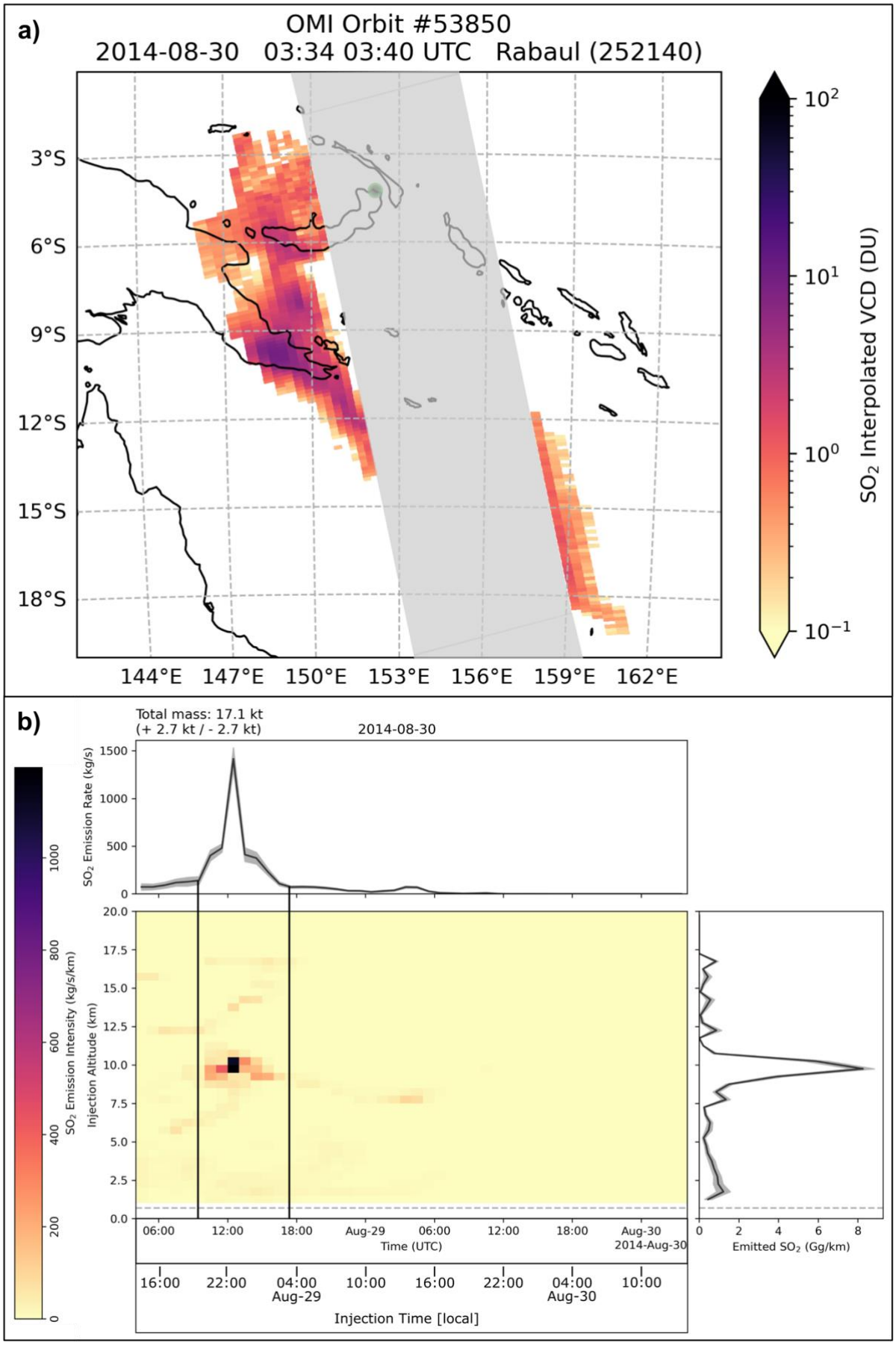
a)
OMI Orbit #53850
2014-08-30 03:34 03:40 UTC Rabaul (252140)
3°S
6°S
9°S
12°S
15°S
18°S
144°E 147°E 150°E 153°E 156°E 159°E 162°E
10^2
10^1
10^0
10^{-1}
SO_2 Interpolated VCD (DU)
b)
Total mass: 17.1 kt
(+ 2.7 kt / - 2.7 kt)
2014-08-30
SO_2 Emission Rate (kg/s)
1500
1000
500
0
SO_2 Emission Intensity (kg/s/km)
1000
800
600
400
200
0
Injection Altitude (km)
20.0
17.5
15.0
12.5
10.0
7.5
5.0
2.5
0.0
06:00 12:00 18:00 Aug-29 06:00 12:00 18:00 Aug-30
Time (UTC)
2014-Aug-30
16:00 22:00 04:00 10:00 16:00 22:00 04:00 10:00
Aug-29 Aug-30
Injection Time [local]
0 2 4 6 8
Emitted SO_2 (Gg/km)

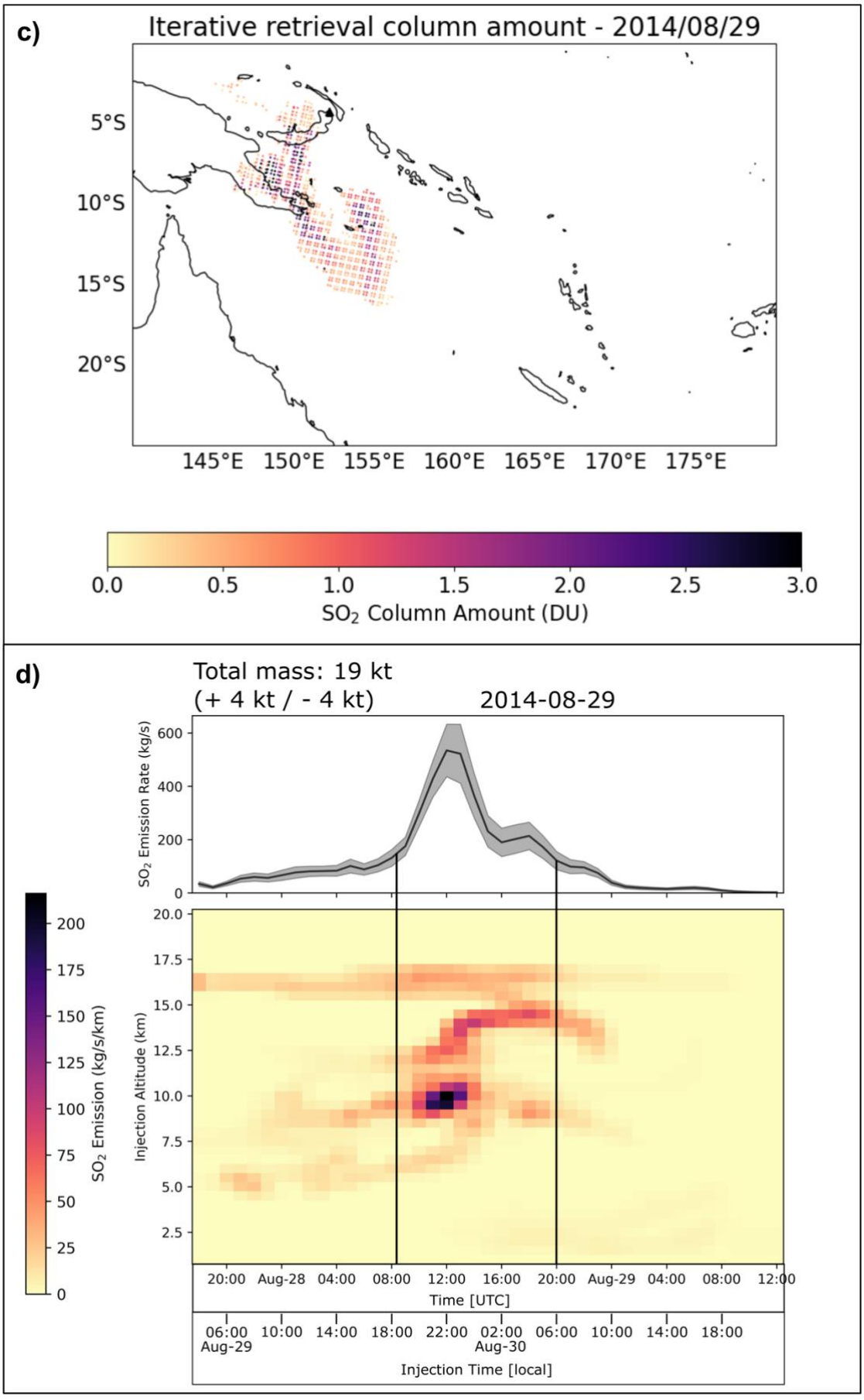
c)
Iterative retrieval column amount - 2014/08/29
5°S
10°S
15°S
20°S
145°E
150°E
155°E
160°E
165°E
170°E
175°E
0.0
0.5
1.0
1.5
2.0
2.5
3.0
SO2 Column Amount (DU)
d)
Total mass: 19 kt
(+ 4 kt / - 4 kt)
2014-08-29
SO2 Emission Rate (kg/s)
600
400
200
0
SO2 Emission (kg/s/km)
200
175
150
125
100
75
50
25
0
Injection Altitude (km)
20.0
17.5
15.0
12.5
10.0
7.5
5.0
2.5
20:00
Aug-28
04:00
08:00
12:00
16:00
20:00
Aug-29
04:00
08:00
12:00
Time [UTC]
06:00
Aug-29
10:00
14:00
18:00
22:00
02:00
Aug-30
06:00
10:00
14:00
18:00
Injection Time [local]

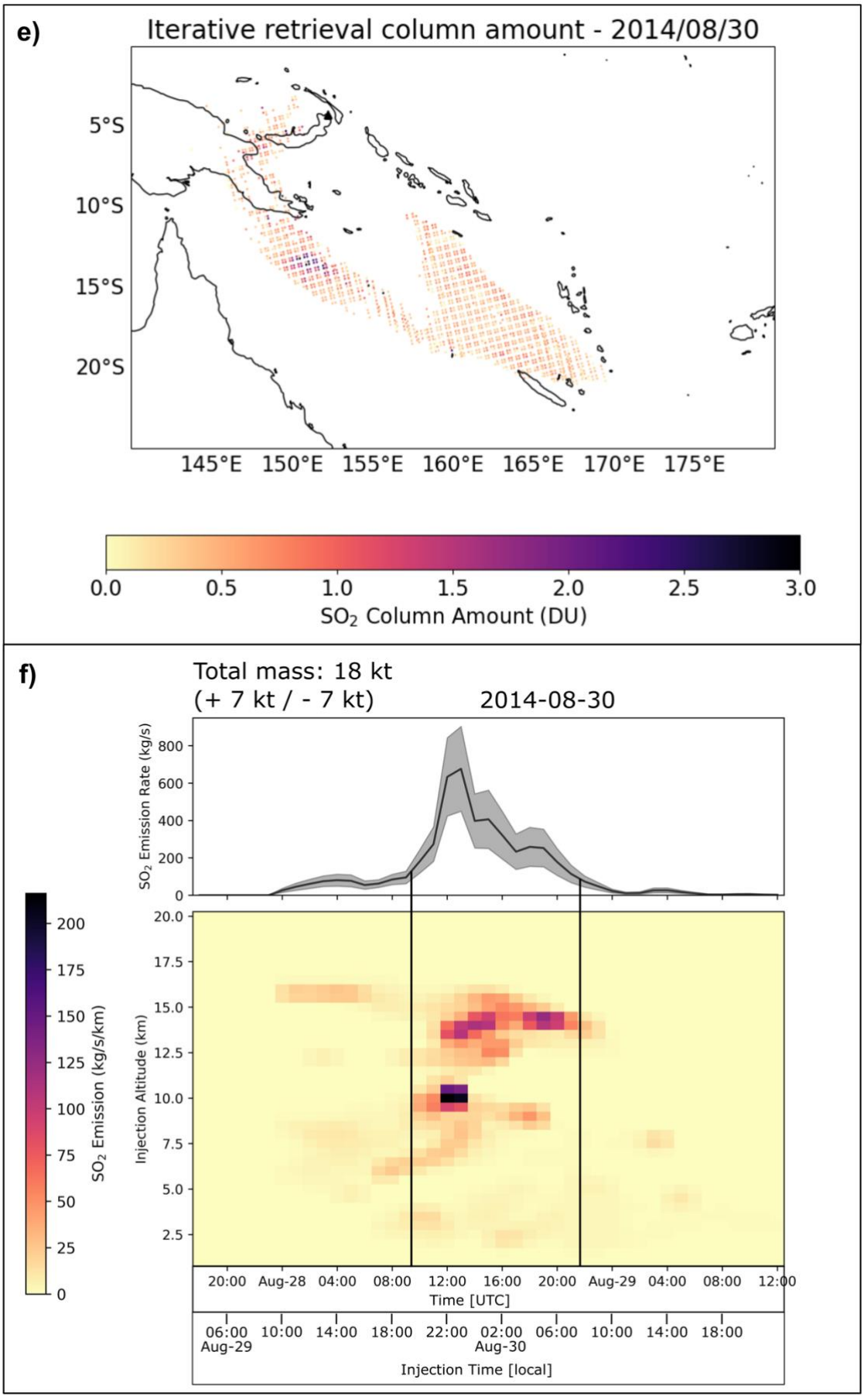
e)
Iterative retrieval column amount - 2014/08/30
5°S
10°S
15°S
20°S
145°E
150°E
155°E
160°E
165°E
170°E
175°E
0.0
0.5
1.0
1.5
2.0
2.5
3.0
SO2 Column Amount (DU)
f)
Total mass: 18 kt
(+ 7 kt / - 7 kt)
2014-08-30
SO2 Emission Rate (kg/s)
800
600
400
200
0
SO2 Emission (kg/s/km)
200
175
150
125
100
75
50
25
0
Injection Altitude (km)
20.0
17.5
15.0
12.5
10.0
7.5
5.0
2.5
20:00
Aug-28
04:00
08:00
12:00
16:00
20:00
Aug-29
04:00
08:00
12:00
Time [UTC]
06:00
Aug-29
10:00
14:00
18:00
22:00
02:00
Aug-30
06:00
10:00
14:00
18:00
Injection Time [local]

Figure 10: a) PlumeTraj image showing the SO_2 plume from the 2014 eruption of Tavurvur during the OMI overpass on 30 August 2014 at 03:34–03:40 UTC (13:34–13:40 local time), ~34 hours after the start of the eruption. The grey bar shows the missing data gap due to the row anomaly. **b)** Satellite-derived SO_2 emission time series for the 2014 eruption using the OMI overpass from 30 August showing a total SO_2 budget for the 2014 Tavurvur eruption of 17.1 ±2.7 kt. The diagrams show the injection altitude (in km), injection time, and SO_2 emissions (in kgs^{-1}) over time. The two black lines in the centre diagram mark the main phase of SO_2 injection (~8 hours). **c)** PlumeTraj image showing the SO_2 plume from the 2014 eruption of Tavurvur during the IASI evening overpass on 29 August 2014 at ~22:44 UTC (~08:00 30 August local time), ~26 hours after the start of the eruption. **d)** Satellite-derived SO_2 emission time series for the 2014 eruption using the IASI overpass from 29 August showing a total SO_2 budget for the 2014 Tavurvur eruption of 19 ±4 kt. The diagrams show the injection altitude (in km), injection time, and SO_2 emissions (in kgs^{-1}) over time. The two black lines in the centre diagram mark the main phase of SO_2 injection (~12 hours). **e)** PlumeTraj image showing the SO_2 plume from the 2014 eruption of Tavurvur during the IASI morning overpass on 30 August 2014 at ~09:45 UTC (~19:45 local time), ~39 hours after the start of the eruption. **f)** Satellite-derived SO_2 emission time series for the 2014 eruption using the IASI overpass from 30 August showing a total SO2 budget for the 2014 Tavurvur eruption of 18 ±7 kt. The diagrams show the injection altitude (in km), injection time, and SO_2 emissions (in kgs^{-1}) over time. The two black lines in the centre diagram mark the main phase of SO_2 injection (~12 hours).

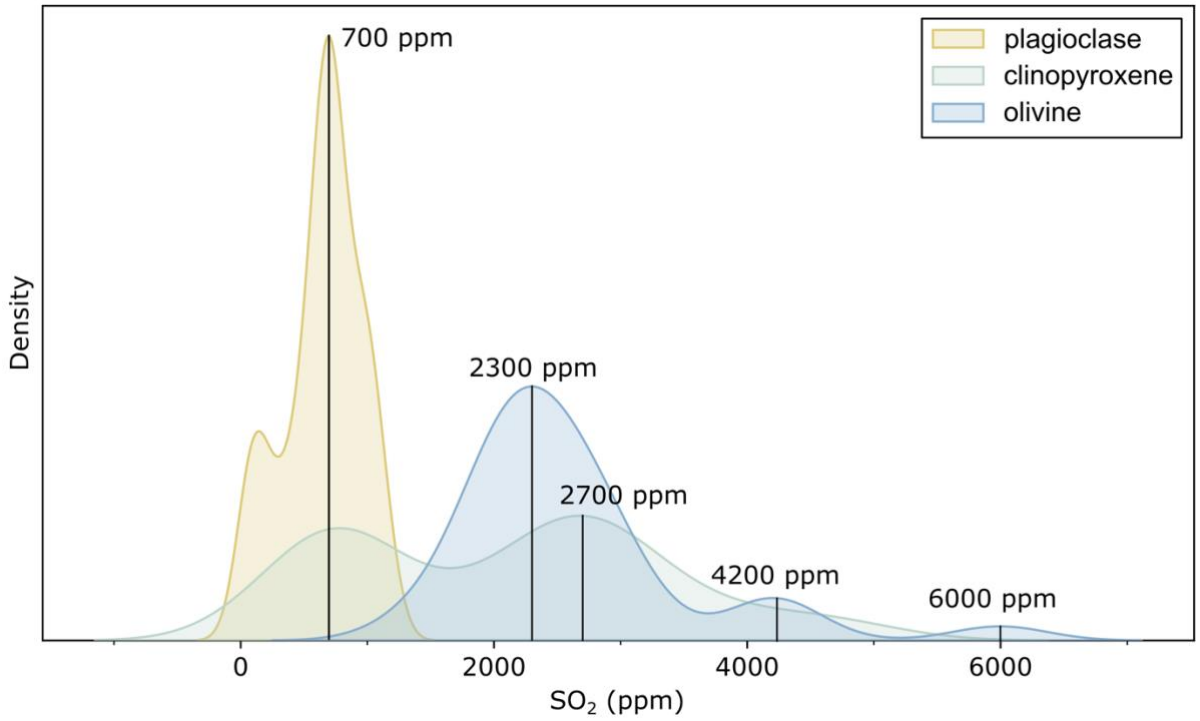

Figure 11: Kernel-density diagram showing the distribution of SO_2 concentrations in the 2014 melt inclusions across the different host minerals.

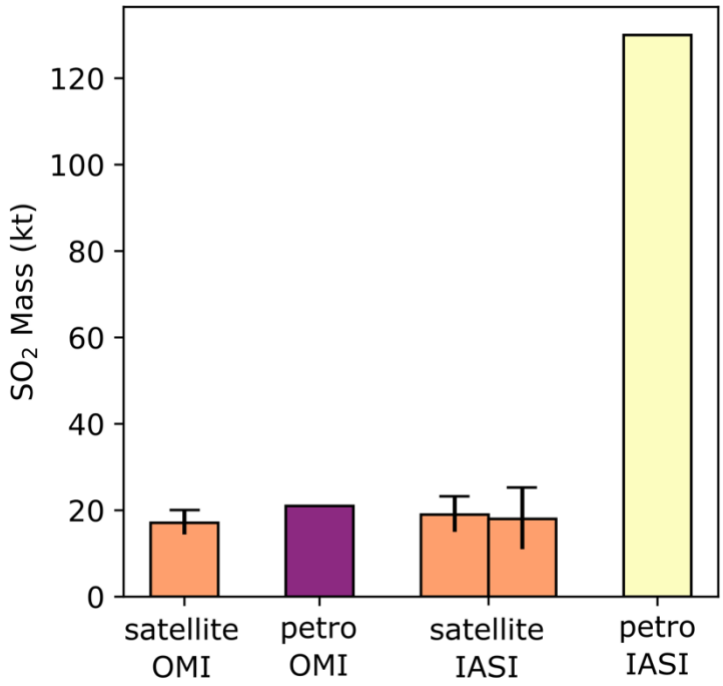

Figure 12: Diagram showing the SO_2 budget for the 2014 eruption of Tavurvur calculated (from left to right) from the OMI satellite overpass from 30 August, from melt inclusion data using the plume height (10 km) and eruption duration (8 hours) from the OMI derived SO_2 emission series, from IASI satellite overpasses from 29 and 30 August, and from melt inclusion data using the plume height (14 km) and eruption duration (12 hours) from the IASI derived SO_2 emission series.

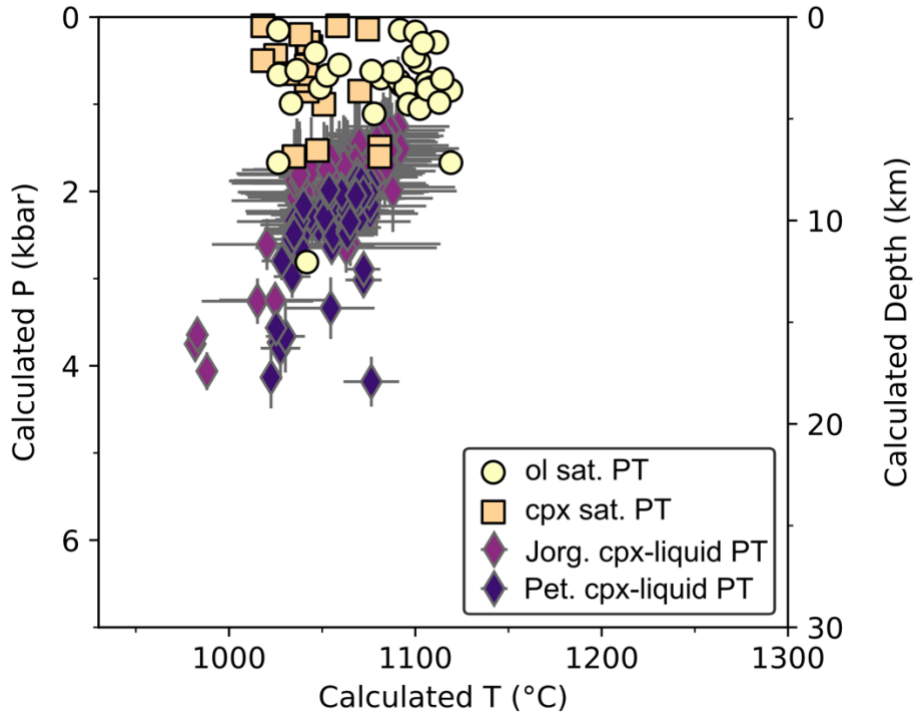

Figure 13: Comparison of saturation pressures for the 2014 olivine-hosted melt inclusions (yellow circles; calculated with VESIcal, Iacovino et al., 2021; MagmaSat model, Ghiorso and Gualda, 2015; olivine thermometer, Putirka, 2008) and for the 2014 clinopyroxene-hosted melt inclusions (orange squares; calculated with VESIcal, Iacovino et al., 2021; MagmaSat model, Ghiorso and Gualda, 2015; clinopyroxene thermometer, Jorgenson et al., 2022) with cpx-liquid thermobarometry results (calculated with thermobar, Wieser et al., 2022; models from Jorgenson et al., 2022, purple diamonds & Petrelli et al., 2020, dark blue diamonds; thermobarometry data from Höhn et al., 2026).

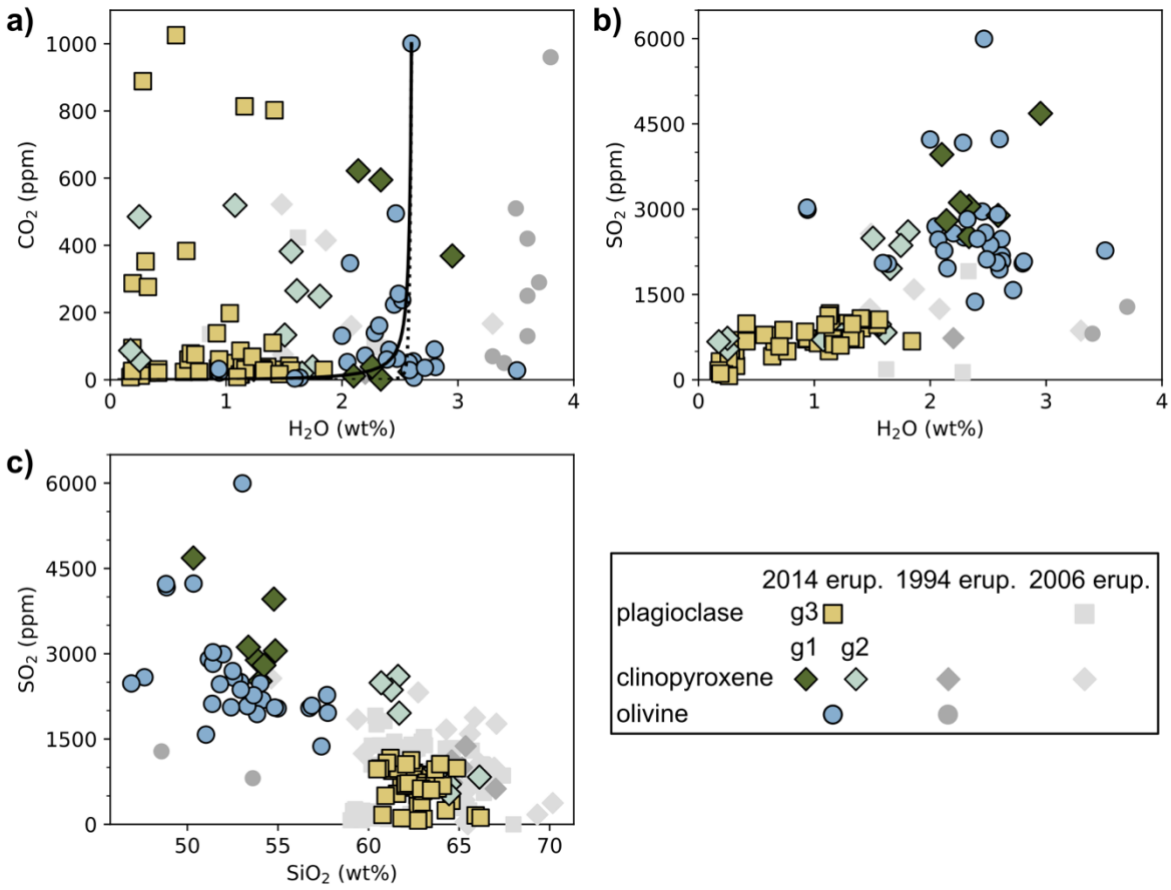

Figure 14: Comparison of volatile contents between 2014 eruption products (coloured symbols) and samples of previous eruptions (grey symbols) (data from Roggensack et al., 1996; Bouvet de Maisonneuve et al., 2015). Shown here are PEC corrected values for the 2006 and 2014 melt inclusions. Black solid and dotted lines represent closed- and open-system degassing paths starting at basaltic olivine-hosted melt inclusion M11_06.10.02.1 calculated with VESIcal (Iacovino et al., 2021) using the MagmaSat model (Ghiorso and Gualda, 2015). g3 = group 3, g1 = group 1, g2 = group 2.

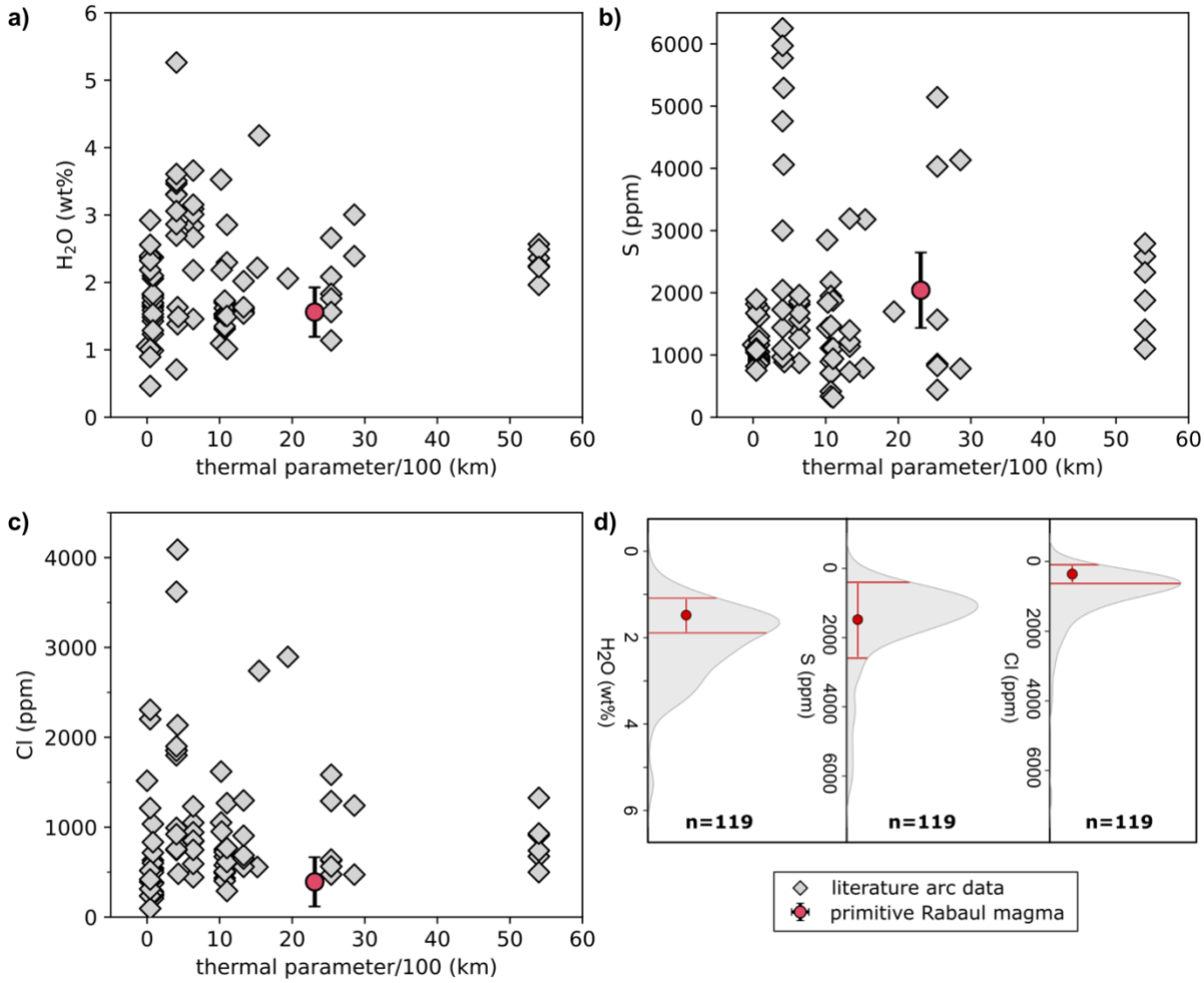

Figure 15: a–c) Comparison of the volatile contents of the primary Rabaul magma with those of primary arc magmas from across the world: every vertical array (at fixed thermal parameter) corresponds to an individual arc with individual points representing volcanoes on the arc (data from Muth and Wallace, 2022). Error bars for the primary Rabaul magma show the range in estimated volatile concentrations. **d)** Kernel-density diagram showing the H_2O, S and Cl contents of the global primary arc spectrum compared to the primary Rabaul magma.